Composition can buffer protein dynamics within liquid-like condensates.

Stela Jelenic[1,2], Janos Bindics[1], Philipp Czermak[1], Balashankar R Pillai[1,2], Martine Ruer[3], Alex S Holehouse[4], Shambaditya Saha[1,5]

[1]Institute of Molecular Biotechnology of the Austrian Academy of Sciences (IMBA), Vienna BioCenter (VBC), Dr. Bohr-Gasse 3, 1030 Vienna, Austria.

[2]Vienna BioCenter PhD Program, Doctoral School of the University of Vienna and Medical University of Vienna, 1030 Vienna, Austria.

[3]Max Planck Institute of Molecular Cell Biology and Genetics, 01307 Dresden, Germany.

[4]Department of Biochemistry and Molecular Biophysics, Washington University School of Medicine, St. Louis, MO 63110, USA.

[5]Correspondence: shambaditya.saha@imba.oeaw.ac.at

Summary

Most non-membrane-bound compartments in cells that form via phase separation have complex composition. Phase separation of individual proteins that form these compartments has been well documented. However, we know relatively little about how the dynamics of individual proteins are modulated in multicomponent systems. Here, we used in vitro reconstitution and in vivo experiments to investigate how complex composition within a liquid-like 'P granule' compartment affects the dynamics of one of its scaffold proteins PGL-3. Using mutational analysis and biophysical perturbations, we generated PGL-3 constructs with reduced alpha-helicity that phase separate in vitro into condensates with widely varying dynamics. We use these PGL-3 constructs to show that introducing other P granule components buffers against large change of dynamics within liquid-like compartments. This dynamics-buffering effect is mediated by weak interactions among two or more components. Such dynamics-buffering may contribute to robust functional output of cellular liquid-like compartments.

Introduction

To organize biochemistry, cells assemble compartments with distinct compositions. Many of these compartments are not enclosed within lipid membranes and assemble via liquid-liquid phase separation (LLPS) of proteins and RNAs from the surrounding cytoplasm or nucleoplasm (Banani *et al*, 2017; Brangwynne *et al*, 2009; Lyon *et al*, 2021). Studies over the past decade have focused on identifying the molecular mechanisms of LLPS within cells. The current model is that LLPS is driven by 'scaffold' proteins and/or RNAs which participate in homotypic or heterotypic interactions with each other to assemble cellular non-membrane-bound compartments (Banani *et al*, 2017, 2016; Lyon *et al*, 2021; Saha *et al*, 2016; Sanders *et al*, 2020; Riback *et al*, 2020). Other macromolecules called 'clients' do not contribute to compartment assembly but concentrate within those compartments and modulate biological function. It is now appreciated that LLPS can be driven by interactions of different types i.e. electrostatic, polar or hydrophobic interactions involving both folded domains and intrinsically disordered regions (Banani *et al*, 2017; Lyon *et al*, 2021). The mechanisms that regulate dynamics of components within these compartments, however, remain unclear.

Macromolecules can phase separate into condensates with different material properties, ranging from liquid-like phases with fast dynamics to dynamically-arrested gels as well as glasses (Banani *et al*, 2017; Jawerth *et al*, 2020). Many liquid-like condensates *in vitro* have also been shown to mature over time, starting as liquid-like droplets that transition into non-dynamic assemblies (Banani *et al*, 2017). The rates of biochemical reactions within biomolecular condensates must depend on the diffusion times of the components. Recent *in vitro* investigations of LLPS for simple two-component systems have shown that the behavior of one component can modulate the dynamics of another within condensates (Boeynaems *et al*, 2019; Rhine *et al*, 2020; Zhang *et al*, 2015; Alshareedah *et al*, 2021). Cellular condensates contain hundreds of different proteins and RNAs. How such complex composition affects dynamics of macromolecules in liquid-like compartments remains poorly understood.

P granules are a canonical liquid-like compartment found in the germline of *C. elegans* (Brangwynne *et al*, 2009). mRNA and over forty proteins are known to concentrate in P

granules (Updike & Strome, 2010). Here, we use in vitro reconstitution and in vivo experiments in adult *C. elegans* gonads to investigate how complex composition within the P granule compartment contributes to the dynamics of one of its scaffold proteins PGL-3 (Saha *et al*, 2016; Hanazawa *et al*, 2011). Using a combination of mutational analysis and biophysical perturbations, we generated PGL-3 constructs that phase separate in vitro into condensates with widely varying dynamics. Investigating the effect of other P granule components on phase separation of PGL-3 constructs, we uncovered a role of complex composition in buffering against large change of dynamics within cellular liquid-like compartments. This “dynamics-buffering” effect is distinct from active processes that depend on ATP hydrolysis, but is mediated by weak interactions among components in liquid-like compartments.

Results

Homotypic and heterotypic interactions drive phase separation of PGL-3 and mRNA at physiological concentrations.

We began by investigating the role of different domains in the phase separation properties of the protein PGL-3 in vitro (Supplementary Fig. 1). Together with other proteins and mRNA, PGL-3 drives the assembly of the canonical liquid-like P granules in the germline of *C. elegans*. Bioinformatic analysis of the 693 residue-long PGL-3 protein predicted that the N-terminus accounting for ~65% of PGL-3 is predominantly α-helical, while the C-terminus accounting for ~35% is mostly disordered (Fig. 1a, Supplementary Fig. 2a, 2b). Consistent with the bioinformatics predictions, circular dichroism (CD) spectroscopy under conditions that do not support phase separation showed that the PGL-3 N-terminal fragment 1-452 is predominantly α-helical, while the C-terminal fragment 370-693 is disordered (Fig. 1f).

Intrinsically disordered polypeptides have in many cases been shown to be necessary and sufficient to drive phase separation. We therefore tested if a recombinantly purified C-terminal fragment of PGL-3 (370-693), can drive phase separation in vitro. To our surprise, we did not observe any phase separation even at high protein concentrations up to ~70 μM (Fig. 1b, c). However, we found that a recombinantly purified N-terminal fragment of PGL-3 (1-452) phase separates into condensates at close to physiological concentrations of PGL-3 (Fig. 1b, c, Supplementary figure 2e). Similar to full-length PGL-3, condensates of the N

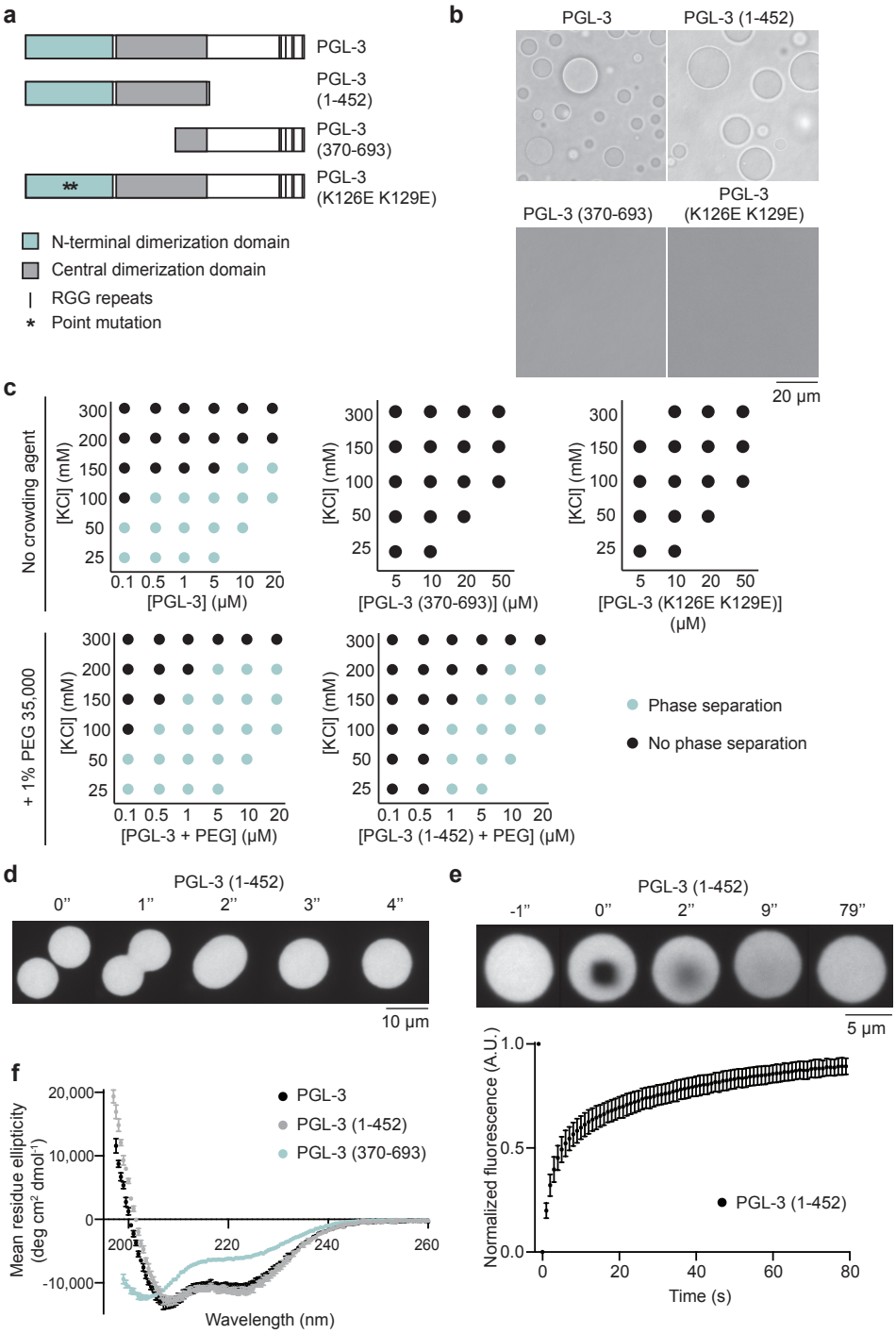

Fig. 1 α-helical N terminus drives phase separation of PGL-3.

a Cartoon representing PGL-3 and mutants. **b** Bright field micrographs of PGL-3 (23 µM), PGL-3 (1-452) (22 µM), PGL-3 (370-693) (67 µM) and PGL-3 (K126E K129E) (108 µM) in 25 mM HEPES pH 7.5, 100 mM KCl, 1mM DTT in absence of crowding agents. Scale bar 20 µm. **c** Phase diagrams of PGL-3 and mutants at different protein and salt (KCl) concentrations. Blue circles represent conditions where phase separation was observed. Black circles represent conditions where phase separation was absent. Top row: Phase diagrams of PGL-3, PGL-3 (370-693), and PGL-3 (K126E K129E) in 25 mM HEPES pH 7.5, 1mM DTT in absence of crowding agents. 5% of the pool of protein was tagged with mEGFP in each case. Bottom row: Phase diagrams of PGL-3, and PGL-3 (1-452) in 25 mM HEPES pH 7.5, 1mM DTT, 1% PEG 35000. 5% of the pool of protein was tagged with mEGFP in each case. **d** Time-lapse fluorescence micrographs show fusion of two PGL-3 (1-452) condensates (5% tagged with mEGFP in 25 mM HEPES pH 7.5, 100 mM KCl, 1mM DTT, 1% PEG 35000). Scale bar 10 µm.

e Time-lapse fluorescence micrographs show fluorescence recovery after photobleaching in a condensate of PGL-3 (1-452) (5% tagged with mEGFP in 25 mM HEPES pH 7.5, 100 mM KCl, 1mM DTT, 1% PEG 35000). Scale bar 5 µm. Shown below is a plot of average normalized fluorescence in bleached regions (1.5 µm x 1.5 µm) of the PGL-3 (1-452) condensates (n = 24) over time. Error bars represent 1 SD.

f Plot of mean residue ellipticity of PGL-3 and mutants vs. wavelength assayed using circular dichroism (CD) spectroscopy. Black circles: PGL-3 (3 µM, 10 mM Potassium phosphate pH 7.5, 300 mM KCl, 1 mM TCEP), Grey circles: PGL-3 (1-452) (3 µM, 10 mM Potassium phosphate pH 7.5, 300 mM KCl, 1 mM TCEP), Blue circles: PGL-3 (370-693) (10 µM, 10 mM Potassium phosphate pH 7.5, 150 mM KCl, 1 mM TCEP). Error bars represent 1 SD among six CD scans.

153 terminal PGL-3 fragment (1-452) are liquid-like in nature. First, condensates are spherical in
154 shape (Fig. 1d, e, Supplementary Fig. 2d). Second, condensates fuse over time to generate
155 a larger condensate (Fig. 1d). Third, fluorescence recovery after photobleaching (FRAP)
156 experiments showed that PGL-3 (1-452) molecules intermix rapidly ($t_{1/2}$ = 4 s) within a
157 condensate (Fig. 1e). We conclude that phase separation of the protein PGL-3 is driven by
158 an α-helical region, while the disordered region may stabilize condensates by modulating
159 the driving forces for phase separation.
160
161 We next investigated how RNA impacts and alters the phase behaviour of PGL-3. It has
162 been previously shown that the PGL-3 protein cannot phase separate independently at
163 physiological concentration (Saha *et al*, 2016). At this concentration, sufficiently long mRNA
164 can trigger phase separation via binding to six arginine-glycine-glycine (RGG) repeats at
165 the C-terminal disordered region of PGL-3 (Saha *et al*, 2016). We therefore expected that
166 when the C-terminal disordered region was mixed with RNA, it would promote phase
167 separation. Unexpectedly, we found that in contrast to full-length PGL-3, mRNA does not
168 support phase separation of the C-terminal disordered region of PGL-3 (Fig. 2a, b). This
169 suggests that the N-terminal α-helical region is essential for phase separation. However, we
170 found that mRNA does not enhance phase separation of the N-terminal α-helical region of
171 PGL-3 either (Fig. 2a, b).
172
173 To investigate the underlying mechanism further, we began by testing if the N-terminal α-
174 helical region of PGL-3 can self-associate. Our analysis using size exclusion
175 chromatography followed by multi-angle light scattering (SEC-MALS) showed that this PGL-
176 3 fragment 1-452 forms a dimer (Supplementary Fig. 2f). Mutation of two residues (K126E
177 K129E) have been shown to interfere with interactions among the N-termini of PGL-3
178 molecules (Aoki *et al*, 2021). We mutated these two residues within the full-length PGL-3
179 protein (K126E K129E) (Fig. 1a) and found that this mutant PGL-3 (K126E K129E) protein
180 cannot phase separate even at high protein concentrations up to ~130 μM (Fig. 1b, c).
181 Addition of mRNA does not trigger phase separation of this protein at physiological
182 concentrations either (Fig. 2a, b). Taken together, our data is consistent with a model where
183 association among folded N-termini of PGL-3 molecules is essential for phase separation.

Fig. 2 Homotypic interaction among PGL-3 molecules is essential for mRNA-dependent phase separation.

a Fluorescence micrographs of PGL-3 and mutants (0.5 μM) in presence or absence of total mRNA (10 ng/μL). 5% of the pool of protein was tagged with mEGFP in each case. Buffer: 25 mM HEPES pH 7.5, 150 mM KCl, 1 mM DTT. 1% PEG 35,000 was added to PGL-3 (1-452). Scale bar 10 μm.
b Plot of the number of condensates with PGL-3 and mutants in presence or absence of total mRNA. For each condition, number of condensates was scored in nine different fluorescence micrographs (116 μm x 117 μm). Error bars represent 1 SD.
c Cartoon showing that at physiological concentrations, mRNA facilitates PGL-3 condensate formation. Association among folded N-termini of PGL-3 molecules is necessary for phase separation.

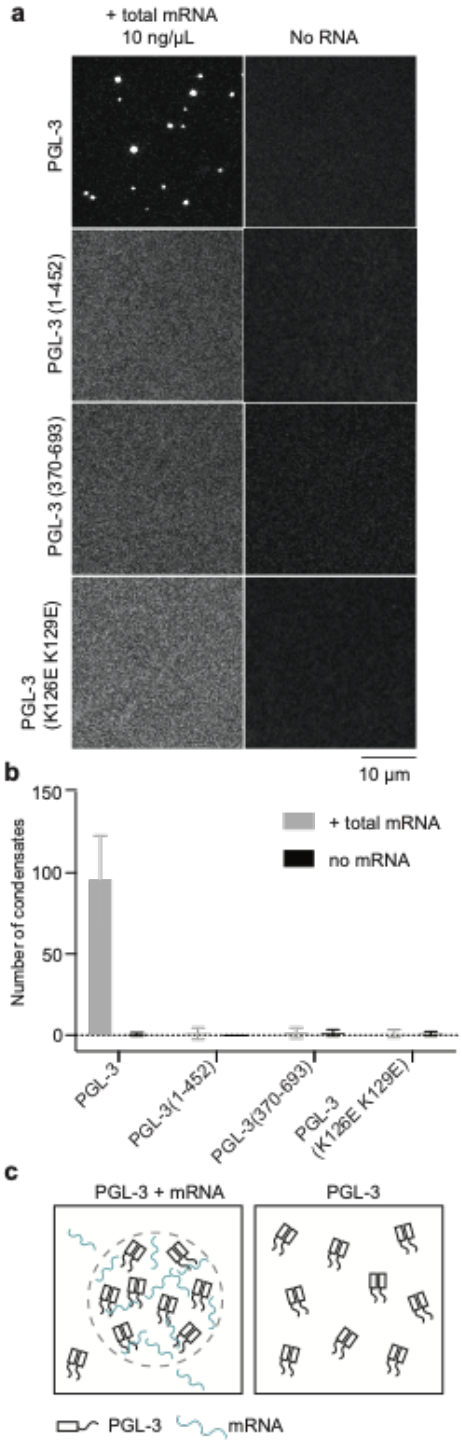

At physiological concentrations, mRNA facilitates this process by binding to the disordered C-terminus of PGL-3 (Fig. 2c).

α-helicity of PGL-3 correlates with dynamics in condensates in vitro.

P granules have a complex composition, containing mRNA and over forty proteins (Updike & Strome, 2010). It is unclear how dynamics within the P granule phase depends on interactions among those components. Two constitutive P granule proteins PGL-1 and GLH-1 have been reported to exchange rapidly between the cytoplasm and liquid-like P granules in *C. elegans* gonads (FRAP half-time ($t_{1/2}$) = 7 – 28 s) (Brangwynne *et al*, 2009). Interestingly, in spite of their vastly reduced compositional complexity, we found that condensates generated in vitro with the PGL-3 protein alone show similar dynamics ($t_{1/2}$ = 7 s) (Supplementary Fig. 2c). To investigate the role of other P granule components on dynamics of PGL-3, we added mRNA and recombinantly purified PGL-1, GLH-1 to condensates of PGL-3 in vitro at physiologically relevant proportions compared to PGL-3 (Saha *et al*, 2016). We found that PGL-1, GLH-1 and mRNA concentrate within condensates of PGL-3 in vitro, but have a modest effect on the dynamics of PGL-3 ($t_{1/2}$ = 10 s) (Supplementary Fig. 2c). This suggests that the dynamics of full length PGL-3 are

223 intrinsic to the protein, and that the influence of complex composition on dynamics is
224 modest.
225
226 In order to address the interactions that drive dynamics within condensates, we began by
227 probing the dynamics of several PGL-3 constructs within phase-separated condensates in
228 vitro. The rate at which molecules of two PGL-3 constructs 1-452 and 1-577, that either lack
229 the disordered C-terminal region entirely or in part, rearrange within condensates are close
230 to full-length PGL-3 (Fig. 1e, Supplementary Fig. 2g, 3a, b). This suggests that interactions
231 involving the disordered C-terminal region of PGL-3 are not essential for the fast dynamics
232 within condensates. Therefore, we addressed the role of the N-terminal α-helical region (1-
233 452) in driving dynamics. In order to avoid engineering mutations that result in significant
234 misfolding of PGL-3 and concomitant loss of its ability to phase separate, we focused our
235 mutational analysis close to the junction of the folded N-terminus and the disordered C-
236 terminus of PGL-3. Surprisingly, we found that a full-length PGL-3 construct (Δ425-452) that
237 lacks only 27 residues phase separates into condensates that are non-dynamic (Fig. 3a, c).
238 Sequence analysis of the PGL-3 protein predicts that this region 425-452 spans two α-
239 helices (one complete helix and fraction of a second helix) (Supplementary Fig. 3d). We
240 generated a PGL-3 construct (hereafter called 'S1') (Fig. 3a) in which the sequence in the
241 region, 425-452, is shuffled while keeping the overall amino acid composition unchanged.
242 We found that S1 phase separates into condensates that are 20- fold less dynamic than
243 with wild-type PGL-3 (Fig. 3d, Supplementary Fig. 3c). Following assembly via phase
244 separation, the extremely slow dynamics in condensates of S1 does not change
245 significantly over 24 h (Supplementary Fig. 3f). Taken together, our data suggests that
246 interactions involving the N-terminal α-helical region of PGL-3 are required for fast
247 dynamics within condensates.
248
249 For more insights into the role of the N-terminal α-helical region in regulating dynamics
250 within condensates of PGL-3, we investigated the contribution of the region 425-452 further.
251 CD spectroscopy showed that α-helicity is reduced in the mutant S1 compared to wild-type
252 PGL-3 (Supplementary Fig. 3g). One possibility is that sequence-shuffling of residues 425-
253 452 changes the tertiary structure of PGL-3. Interestingly, we found that the mutant S1 can
254 phase separate at concentrations lower than wild-type PGL-3 (Supplementary Fig. 3e).

255 Further, mutation of two residues (K126E K129E), that interfere with interactions among the
256 N-termini of wild-type PGL-3 molecules (Aoki *et al*, 2021), also inhibit phase separation of
257 the S1 mutant even at high protein concentrations up to ~50 μM (Fig. 3a, Supplementary
258 Fig. 3c, e). This suggests that, regardless of change in tertiary structure, interactions among
259 the N-termini of S1 molecules are important for phase separation. In order to address the
260 consequence of sequence-shuffling of residues 425-452 further, we compared the
261 structural stability of S1 with wild-type PGL-3. We tested this through thermal unfolding
262 which monitor α-helical content between 20 °C and 90 °C, using the CD signal at 222 nm
263 as a measure of α-helical content. We found that wild-type PGL-3 unfolds in two phases as
264 temperature is increased (T_m = 47 °C and 61 °C) (Fig. 3b). On the other hand, S1 also
265 unfolds in two phases but sequence-shuffling results in lower thermostability (T_m = 41 °C
266 and 61 °C) (Fig. 3b). Taken together, our observations on the phase separation behavior of
267 the S1 mutant raises the possibility that loss of α-helicity of PGL-3 may correlate with
268 slower dynamics in condensates.
269
270 In order to address if dynamics in condensates correlate with structural stability of PGL-3,
271 we compared the dynamics of condensates formed via phase separation of folded and
272 unfolded PGL-3 constructs. Heat-induced unfolding of both PGL-3 and S1 is irreversible
273 (Supplementary Fig. 3h, i). These constructs do not recover lost α-helicity once the
274 temperature is lowered to 21 °C following unfolding at higher temperatures. Therefore, we
275 heated mEGFP-tagged PGL-3 and S1 proteins at different temperatures for 10 min followed
276 by cooling to room temperature and triggering phase separation (by diluting salt (KCl)
277 concentration to 150 mM). Wild-type PGL-3 does not lose α-helicity when heated to 43.5 °C
278 (Supplementary Fig. 3h). We observed that PGL-3-mEGFP preheated at 43.5 °C generates
279 condensates that are liquid-like (Fig. 3e). On the other hand, heating S1 to 43.5 °C results
280 in partial unfolding (Supplementary Fig. 3i), and phase separation of this partially unfolded
281 S1-mEGFP protein generates solid-like condensates with no observable FRAP recovery
282 (Fig. 3f). Similarly, heating wild-type PGL-3 to a higher temperature (50 °C) results in partial
283 unfolding (Supplementary Fig. 3h), and phase separation of this partially unfolded PGL-3-
284 mEGFP protein generates solid-like condensates with no observable FRAP recovery (Fig.
285 3e). Taken together, our data suggests that reduced α-helicity of PGL-3 correlates with
286 slower dynamics in condensates.

Fig. 3 α-helicity of PGL-3 correlates with dynamics in condensates.

a Cartoon representing PGL-3, S1, S1(K126E K129E) and PGL-3 (Δ425-452). Residues 425-452 of wild-type PGL-3 are shuffled in mutants S1 and S1(K126E K129E) .
b Plot of normalized circular dichroism (CD) spectroscopy signal at 222 nm with PGL-3 (black circle) and S1 (blue circle) vs. temperature, assayed at 5 μM protein concentration in 25 mM HEPES pH 7.5, 1 M KCl, 1 mM DTT. Error bars represent 1 SD among three independent measurements. Arrows highlight 43.5 °C and 50 °C – temperatures where partial unfolding of PGL-3 begins and ends respectively.
c-d Time-lapse fluorescence micrographs show fluorescence recovery after photobleaching in condensates of **c** PGL-3 (Δ425-452)-mEGFP or **d** S1 (5% of the pool of protein was tagged with mEGFP). Arrowheads show photobleached area in condensates of PGL-3 (Δ425-452)-mEGFP. Scale bars 5 μm. Shown below the time-lapse micrographs are plots of average normalized fluorescence over time **c** in bleached regions (1.4 μm x 1.4 μm) of PGL-3 (Δ425-452)-mEGFP condensates (n = 8) or **d** in bleached regions (1.5 μm x 1.5 μm) of S1 (5% tagged with mEGFP) condensates (n = 18). Error bars represent 1 SD.
e Time-lapse fluorescence micrographs show fluorescence recovery after photobleaching at room temperature in condensates of PGL-3-mEGFP (preheated at 43.5 °C or 50 °C). Scale bar 5 μm. Shown next to the micrographs is a plot of average normalized fluorescence over time in bleached regions (1.4 μm x 1.4 μm) within the condensates of PGL-3-mEGFP preheated at 43.5 °C (black circles, n =8) or 50 °C (grey circles, n = 8). Error bars represent 1 SD.
f Time-lapse fluorescence micrographs show fluorescence recovery after photobleaching at room temperature in condensates of S1-mEGFP (preheated at 43.5 °C). Scale bar 5 μm. Shown next to the micrographs is a plot of average normalized fluorescence over time in bleached regions (1.4 μm x 1.4 μm) within the condensates of S1-mEGFP preheated at 43.5 °C (n =8). Error bars represent 1 SD.

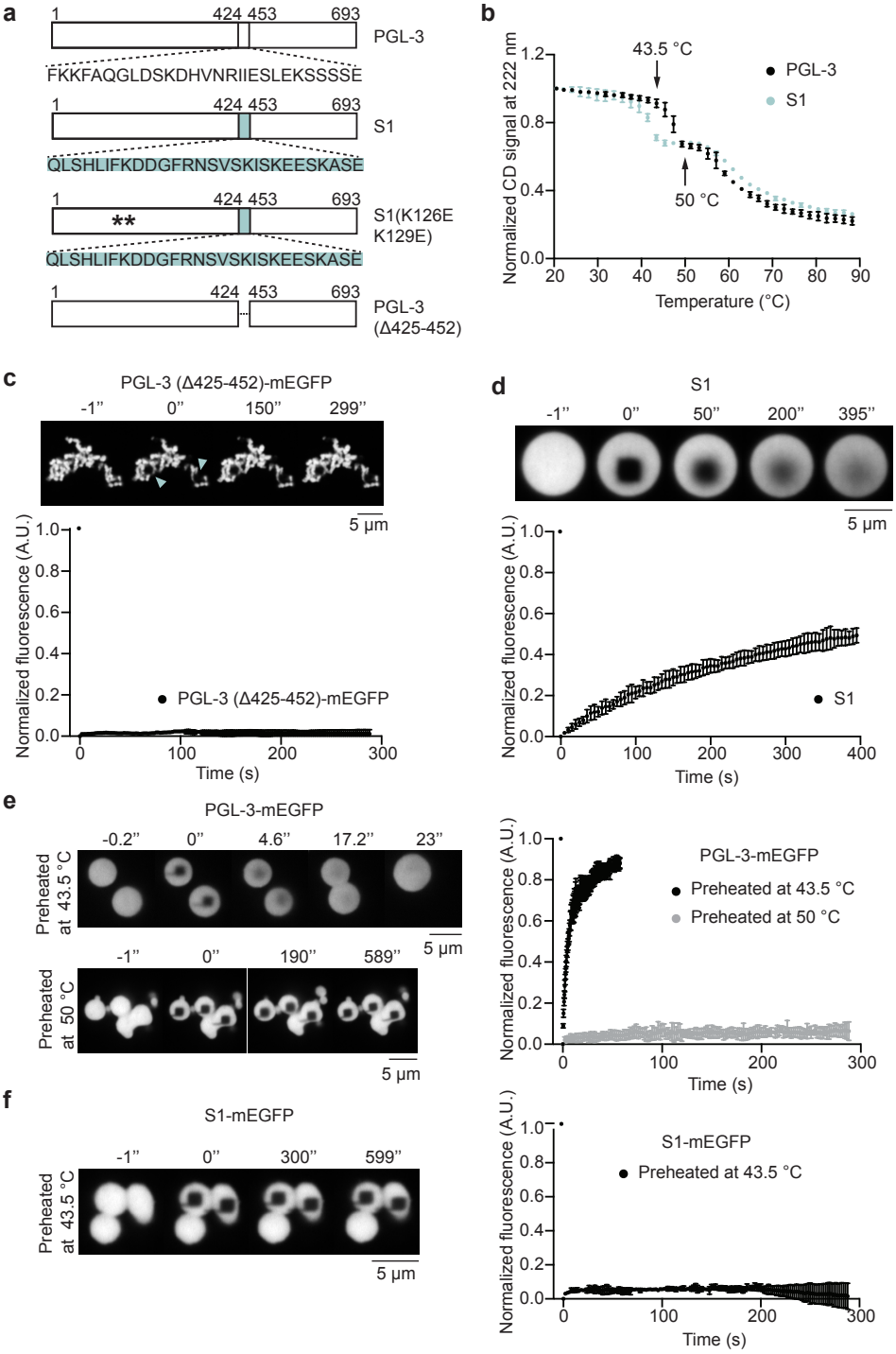

342 **P granule components buffer against reduced dynamics in condensates.**
343 We wanted to see if similar changes in dynamics are seen in P granules in *C. elegans*
344 worms. To address this, we injected mEGFP-tagged wild-type PGL-3 or S1 proteins into
345 gonads of adult *C. elegans* and investigated their dynamics. Both PGL-3-mEGFP and S1-
346 mEGFP target to perinuclear P granules (Fig. 4a). Fluorescence recovery after
347 photobleaching experiments showed that S1 exchanges between P granules and
348 cytoplasm at rates similar to wild-type PGL-3 (Fig. 4b). Similarly, when partially unfolded
349 PGL-3-mEGFP (preheated at 50 °C) is injected into gonads of adult *C. elegans*, this protein
350 concentrates in perinuclear P granules (Fig. 4a) and exchanges between P granules and
351 cytoplasm at rates similar to wild-type PGL-3 (Fig. 4b). These suggest that the
352 multicomponent P granule phase can prevent slowdown of dynamics associated with
353 reduced α-helicity of PGL-3.
354
355 To reconstitute the multicomponent nature of the P granule, we purified and added back
356 other P granule proteins to the PGL-3 phase formed in vitro. Interestingly, addition of
357 merely a few P granule components (mRNA and recombinantly purified PGL-1 and GLH-1)
358 to condensates of S1 in vitro enhances the dynamics of S1 almost 20-fold to match the
359 dynamics observed in condensates of wild-type PGL-3 (Fig. 4c, Supplementary Fig. 4b, c,
360 5f). Further, we found that dynamics within condensates of S1 can be significantly
361 enhanced simply by adding wild-type PGL-3 protein (Supplementary Fig. 5a). For better
362 insight into how the PGL-3 protein supports fast dynamics of S1, we added three different
363 PGL-3 constructs (the N-terminal α-helical fragment 1-452, the C-terminal fragment 370-
364 693, and the phase separation-incompetent mutant PGL-3 (K126E K129E)) at different
365 concentrations to condensates of S1. We found that all three PGL-3 constructs concentrate
366 within condensates of S1 to different degrees (Supplementary Figure 5c) and enhance the
367 dynamics of S1 (Supplementary Fig. 5a). Further, addition of the phase separation-
368 incompetent mutant S1 (K126E K129E) to condensates of S1 also enhanced the dynamics
369 of S1 within condensates (Supplementary Fig. 5a and 5c). Taken together, our data
370 suggests that enhanced S1 dynamics in condensates can be supported by a wide variety of
371 interactions involving other P granule components (PGL-1, GLH-1, mRNA) or different parts
372 of the PGL-3 protein.
373

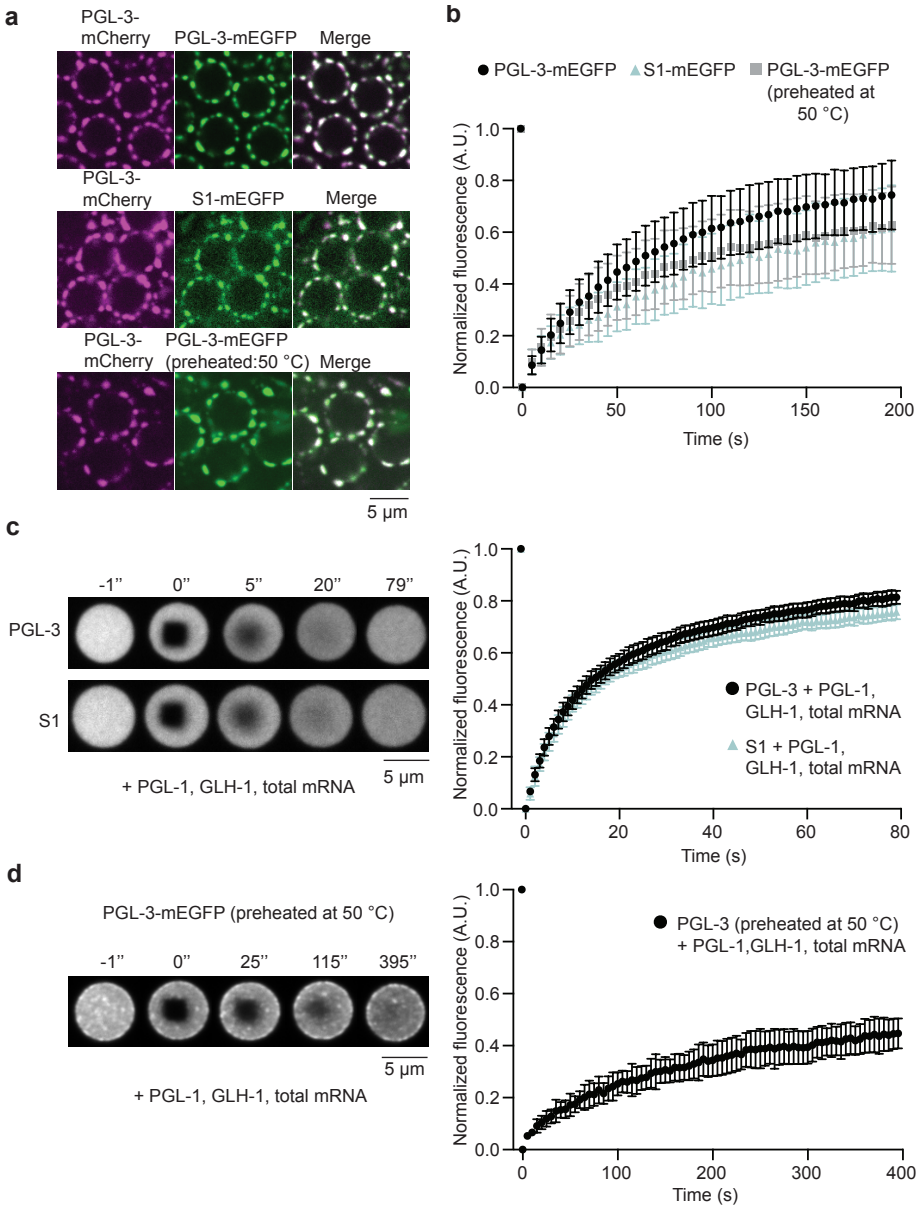

Fig. 4 P granule components promote fast dynamics of PGL-3 constructs with reduced α-helicity.

a Fluorescence micrographs of gonads in *C. elegans* expressing PGL-3-mCherry (shown in magenta) injected with recombinantly-purified PGL-3-mEGFP, S1-mEGFP, or PGL-3-mEGFP preheated at 50 °C (shown in green). A single confocal section is shown. Scale bar 5 µm.
b Plot showing average normalized fluorescence signal over time in bleached peri-nuclear regions (1.5 µm x 1.5 µm) in wild-type *C. elegans* gonads injected with recombinantly purified PGL-3-mEGFP (black circles, n = 46), S1-mEGFP (blue triangles, n = 36), or PGL-3-mEGFP preheated at 50 °C (grey circles, n = 37). Error bars represent 1 SD. For each condition, data from 2 different animals injected with a recombinantly purified protein were analyzed.
c Time-lapse fluorescence micrographs show fluorescence recovery after photobleaching over time in condensates of PGL-3 (5 µM) or S1 (5 µM) (5% of the pool of protein was tagged with mEGFP) in presence of PGL-1 (6.7 µM), GLH-1 (1 µM), and total mRNA (14 ng/µL). Scale bar 5 µm. Shown next to the micrographs is a plot of average normalized fluorescence over time in bleached regions (1.5 µm x 1.5 µm) within the condensates of PGL-3 (black circles, n = 20) or S1 (blue triangles, n = 21) in presence of PGL-1, GLH-1 and total mRNA. Error bars represent 1 SD.
d Time-lapse fluorescence micrographs show fluorescence recovery after photobleaching over time in a condensate of PGL-3-mEGFP preheated at 50 °C (1 µM) in presence of PGL-1 (6.7 µM), GLH-1 (1 µM), and total mRNA (14 ng/µL). Scale bar 5 µm. Shown next to the micrographs is a plot of average normalized fluorescence over time in bleached regions (1.5 µm x 1.5 µm) within the condensates of PGL-3-mEGFP preheated at 50 °C (n = 14). Error bars represent 1 SD.

We next wondered if addition of other P granule components is able to support or rescue a dynamic state of partially unfolded PGL-3 within condensates. In contrast to S1, which generates condensates that are liquid-like, partially unfolded PGL-3-mEGFP (preheated at

427 50 °C) phase separates into non-dynamic solid-like condensates in vitro (Fig. 3e). We
428 tested the ability of different components to rescue dynamics of partially unfolded PGL-3-
429 mEGFP. When P granule components (mRNA and recombinantly purified PGL-1 and GLH-
430 1) are added to partially unfolded PGL-3-mEGFP at concentrations similar to those used
431 with S1, the PGL-3 protein phase separates predominantly into non-dynamic condensates
432 (Supplementary Fig. 4a, d, e). However, when a lower concentration of the partially
433 unfolded PGL-3 protein is used, addition of these P granule components supports its phase
434 separation into liquid-like condensates (Fig. 4d). These results revealed a concentration-
435 dependence to the extent with which unfolded PGL-3 impacts condensate dynamics.
436
437 We wondered if, similar to partially unfolded PGL-3-mEGFP, the dynamics of S1 also
438 depends on its concentration. In the assays in which S1 is mixed with different additional
439 components, 5% of the total pool of S1 is tagged with mEGFP. This allowed us to measure
440 the dynamics of S1 within condensates using FRAP. Following photobleaching,
441 fluorescence recovered in bleached region within condensates in two phases – a fast phase
442 driven predominantly by internal rearrangement of molecules within the condensate, and a
443 slower phase driven by the exchange with the pool of unbleached molecules outside the
444 condensate (Supplementary Fig. 6a-f). We focused on the fast phase of recovery and used
445 single-exponential fits to estimate half-time of internal rearrangement of S1 molecules
446 within condensates of different composition. On addition of other P granule components
447 (PGL-1, GLH-1, mRNA) to different concentrations of S1, we found that the half-time of
448 FRAP recovery of S1 within condensates remains relatively unchanged in spite of almost 5-
449 fold change in mEGFP-fluorescence signal per unit area within the condensates (Fig. 5a).
450 Assuming that mEGFP-fluorescence reports on the concentration of S1, this observation
451 suggests that P granule components can buffer the dynamics of S1 close to rates observed
452 in condensates of wild-type PGL-3 alone (Fig. 5a, d). However, the dynamics of S1 slows
453 down above a threshold concentration (9 μM in Fig. 5a), suggesting that P granule
454 components can buffer the dynamics of S1 only within a range of concentrations in
455 condensates. We wondered if the observed dynamics buffering effect within condensates of
456 S1 is limited to the specific set of additives PGL-1, GLH-1 and mRNA. We assayed this by
457 adding to condensates of S1 the construct PGL-3 (K126E K129E). The mutations K126E
458 K129E are expected to interfere with interactions among N-termini of S1 and PGL-3 (K126E

459 K129E) molecules (Aoki *et al*, 2021). We found that addition of this phase separation-
460 incompetent mutant PGL-3 (K126E K129E) can also buffer dynamics within a 2- fold range
461 of S1 concentration within condensates (Fig. 5b). However, the buffering is different
462 compared to when PGL-1, GLH-1 and mRNA are added. Specifically, the range of
463 concentrations of S1 in condensates where dynamics is buffered and the associated half-
464 time of FRAP recovery depend on the additives. We used condensates of similar size for
465 our analysis (average $\pm$ 1 SD of diameter of condensates are 6.4 $\pm$ 1.7 μm (Fig. 5a) and 5.9
466 $\pm$ 0.4 μm (Fig. 5b)). Therefore, dynamics buffering here is likely to represent similar
467 diffusion rates of S1 within condensates.
468
469 For more insights into how addition of different components rescues slowdown of S1
470 dynamics within condensates, we added wild-type PGL-3, or different PGL-3 or S1
471 constructs to condensates of S1. These additives titrated the concentration of S1 within
472 condensates (tracked by S1-mEGFP fluorescence signal per unit area) over a range
473 spanning concentration observed with condensates of S1 alone and those in presence of
474 other P granule components (PGL-1, GLH-1, mRNA). Here, we found that the half-time of
475 FRAP recovery of S1 correlates with mEGFP-fluorescence signal per unit area within the
476 condensates (Fig. 5c). This suggests that, regardless of the condensate composition, fast
477 dynamics generally correlate with smaller concentrations of S1. In control assays, we found
478 that the dynamics of the wild-type PGL-3 protein does not correlate significantly with either
479 concentration of PGL-3 or the composition of the condensate (Fig. 5d, Supplementary Fig.
480 5b, d).
481

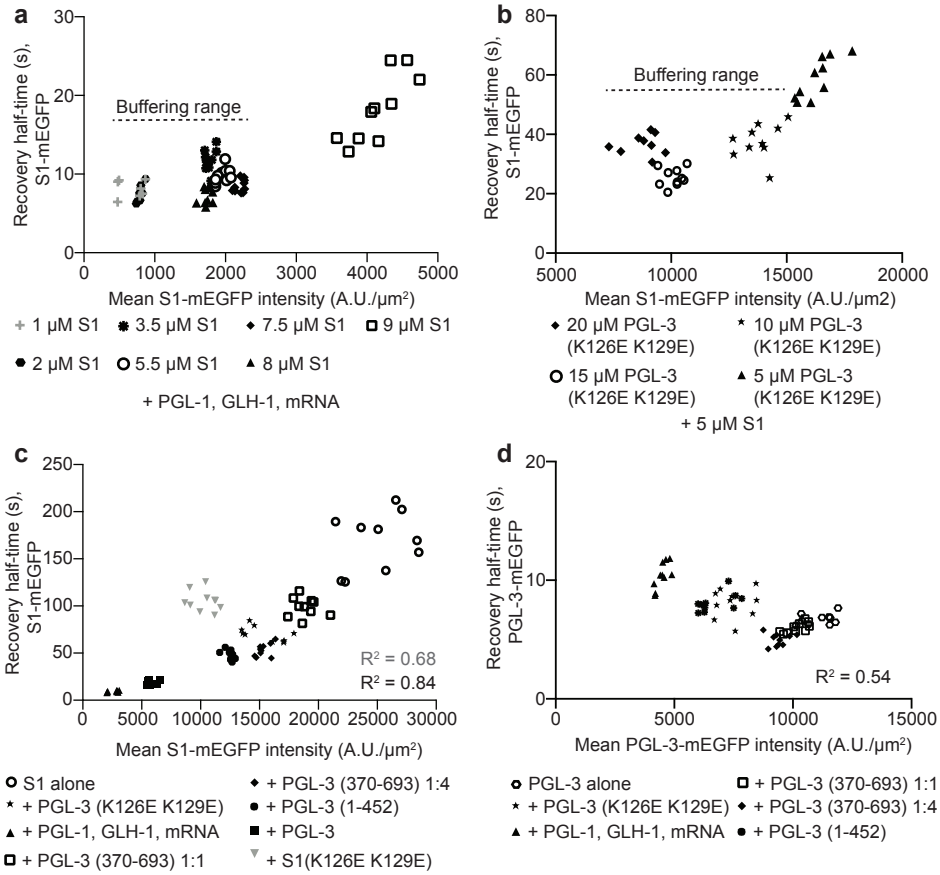

Fig. 5 Dynamics of S1 in condensates of different composition.

Analysis of fluorescence recovery after photobleaching within 1.5 μm x 1.5 μm regions in condensates of different composition. Half-time of fluorescence recovery after photobleaching ($t_{1/2}$) in each case was estimated by fitting the data to a single-exponential curve (see methods section for details). **a** Plot of $t_{1/2}$ vs. mean S1-mEGFP fluorescence intensity per unit area (before photobleaching) within condensates. Each point on the plots represents data from a single photobleached region within a condensate of defined composition which includes 5 μM PGL-1, 0.75 μM GLH-1, 11 ng/ μM mRNA and different S1 concentrations indicated as follows. Grey plus: 1 μM S1, solid hexagon: 2 μM S1, asterisk 3.5 μM S1, open circle: 5.5 μM S1, solid diamond: 7.5 μM S1, solid triangle: 8 μM S1, open square: 9 μM S1. Ten points are plotted for each composition (seven for 1 μM S1) and buffering range indicates a range of S1 concentrations where $t_{1/2}$ does not differ significantly between different conditions.
b Plot of t1/2 vs. mean S1-mEGFP fluorescence intensity per unit area (before photobleaching) within condensates. Each point on the plots represents data from a single photobleached region within a condensate of defined composition which includes 5 μM S1 and different concentrations of PGL-3 (K126E K129E) indicated as follows. Solid diamond: 20 μM PGL-3 (K126E K129E), open circle: 15 μM PGL-3 (K126E K129E), asterisk 10 μM PGL-3 (K126E K129E), solid triangle: 5 μM PGL-3 (K126E K129E), Ten points are plotted for each composition (nine for 20 μM PGL-3 (K126E K129E)) and buffering range indicates a range of S1 concentrations where t1/2 does not differ significantly between different conditions.
c Plot of $t_{1/2}$ vs. mean S1-mEGFP fluorescence intensity per unit area (before photobleaching) within condensates. Each point on the plots represents data from a single photobleached region within a condensate of defined composition as follows. Open circle: S1 alone (10 μM, 5% mEGFP-tagged), solid diamond: S1 (5 μM, 5% mEGFP-tagged) + PGL-3 (370-693) (20 μM), solid asterisk: S1 (5 μM, 5% mEGFP-tagged) + PGL-3 (K126E K129E) (5 μM), solid circle: S1 (5 μM, 5% mEGFP-tagged) + PGL-3 (1-452) (5 μM), solid triangle: S1 (5 μM, 5% mEGFP-tagged) + PGL-1 (6.7 μM) + GLH-1 (1 μM) + total mRNA (14 ng/μL), solid square: S1 (5 μM, 5% mEGFP-tagged) + PGL-3 (5 μM), open square: S1 (5 μM, 5% mEGFP-tagged) + PGL-3 (370-693) (5 μM), grey inverse triangle: S1 (5 μM, 5% mEGFP-tagged) + S1(K126E K129E) (5 μM). Ten points are plotted for each composition. All or part of the data were fit using linear regression (R^2 = 0.68, fit of all data; R^2 = 0.84, fit of data on all compositions excluding S1+ S1(K126E K129E)). Data points for S1+ S1(K126E K129E) are highlighted since S1(K126E K129E) is the only construct added to S1 which contains the shuffled 425-452 region.
d Plot of $t_{1/2}$ vs. mean PGL-3-mEGFP fluorescence intensity per unit area (before photobleaching) within condensates. Each point on the plots represents data from a single photobleached region (1.5 μm x 1.5 μm) within a condensate of defined composition as follows. Open hexagon: PGL-3 alone (10 μM, 5% mEGFP-tagged), open square: PGL-3 (5 μM, 5% mEGFP-tagged) + PGL-3 (370-693) (5 μM), solid asterisk: PGL-3 (5 μM, 5% mEGFP-tagged) + PGL-3 (K126E K129E) (5 μM), solid diamond: PGL-3 (5 μM, 5% mEGFP-tagged) + PGL-3 (370-693) (20 μM), solid triangle: PGL-3 (5 μM, 5% mEGFP-tagged) + PGL-1 (6.7 μM) + GLH-1 (1 μM) + total mRNA (14 ng/μL), solid circle: PGL-3 (5 μM, 5% mEGFP-tagged) + PGL-3 (1-452) (5 μM). Ten points are plotted for each composition and R^2 value for a linear regression fit among all compositions is indicated.

538

539 **Discussion**

540 To maintain homeostasis, cellular liquid-like compartments must be functionally robust
541 against small changes in composition or denaturation of one or more of its components.
542 The mechanisms that provide such robustness remain unclear. A recent study proposed
543 that liquid-liquid phase separation may reduce variation in concentration of components
544 within condensates (Klosin *et al*, 2020). It remains unclear if LLPS can similarly buffer
545 diffusion rate of components within condensates. Recent studies with simple two-
546 component LLPS systems showed that the behavior of one component can influence the
547 dynamics of another within condensates (Boeynaems *et al*, 2019; Rhine *et al*, 2020; Zhang
548 *et al*, 2015; Alshareedah *et al*, 2021). While components are expected to influence the
549 dynamics of each other within multi-component condensates, it is unclear *a priori* how
550 dynamics of biomolecular condensates with complex composition adapt to
551 misfolding/denaturation of one or more component proteins. Here, we show that the liquid-
552 like P granule phase can rescue slow-down of diffusion rate associated with denaturation of
553 a component protein. Such dynamics-buffering may contribute to functional robustness of
554 cellular liquid-like compartments.

555

556 In order to understand how composition supports dynamics-buffering in biomolecular
557 condensates, we began by addressing why denaturation of the PGL-3 protein leads to
558 slower dynamics in condensates. One possibility is that the conformational changes of
559 PGL-3 associated with reduced α-helicity facilitate stronger inter-molecular interactions. For
560 instance, loss of α-helicity could increase the valence of “stickers” leading to additional
561 physical crosslinks among PGL-3 molecules (Choi *et al*, 2020). Stronger inter-molecular
562 interactions could inhibit rapid rearrangement of interacting partners within condensates,
563 resulting in slower dynamics. Alternatively, interactions involving unfolded or partially
564 unfolded PGL-3 molecules could generate inter-polypeptide chain entanglements within
565 condensates resulting in slower dynamics. With diffusion of PGL-3 molecules within
566 condensates, more entanglements could develop over time resulting in further decrease in
567 dynamics. Few observations suggest that slower dynamics within PGL-3 condensates
568 result predominantly from stronger inter-molecular interactions in contrast to inter-chain
569 entanglements. First, dynamics of the mutant S1 protein within condensates does not

570 change significantly over 24 h. Second, the mutations K126E K129E that interfere with
571 interactions among PGL-3 or S1 molecules (Aoki *et al*, 2021) help enhance dynamics of S1
572 molecules within condensates. For instance, when added to condensates of S1, both S1
573 (K126E K129E) and PGL-3 (K126E K129E) help enhance the dynamics of S1 within
574 condensates. Addition of S1 (K126E K129E) reduces concentration of S1 within
575 condensates more than addition of PGL-3 (K126E K129E). However, dynamics of S1 within
576 condensates is faster in spite of higher concentration with PGL-3 (K126E K129E). Taken
577 together, these observations support the model that slow dynamics of S1 within
578 condensates depend on interactions among S1 molecules and suggest that interaction
579 among S1 molecules is stronger than that between wild-type PGL-3 molecules. Stronger
580 interaction among S1 molecules is further supported by the observation that S1 molecules
581 can phase separate at lower concentrations compared to wild-type PGL-3 molecules
582 (Supplementary Fig. 3e).
583
584 Our data is consistent with the model that other regions of S1 molecules cooperate with
585 residues 425-452 (shuffled) to generate stronger inter-molecular interactions. For instance,
586 addition of the mutant S1 (K126E K129E) enhances dynamics of S1 within condensates in
587 contrast to maintaining the slower dynamics observed within condensates of S1 alone. This
588 suggests that the interactions disrupted by the mutations K126E and K129E also contribute
589 to slow S1 dynamics. One possibility is that interactions involving the residues K126 and
590 K129 favor S1 conformations that enhance 425-452 (shuffled)-dependent interactions.
591 Indeed, the mutations K126E K129E have been reported to interfere with interactions
592 among N-termini of PGL-3 molecules (Aoki *et al*, 2021). While two self-association domains
593 within the α-helical N-terminus of PGL-3 have been mapped (Aoki *et al*, 2021, 2016),
594 structural insights into those associations are limited. However, PGL-3 shares significant
595 sequence similarity with another protein PGL-1. Crystal structures are available for
596 fragments of the PGL-1 protein that show the two self-association domains at the N-
597 terminus are predominantly α-helical and globular in nature (Aoki *et al*, 2016, 2021).
598 Therefore, one possibility is that shuffling the sequence 425-452 of PGL-3 or heat-induced
599 unfolding of PGL-3 exposes hydrophobic residues that become available to participate in
600 inter-molecular interactions. This effect may be enhanced within phase separated
601 condensates if the local solvent environment favors more extended conformations of the

602 PGL-3 protein, allowing more inter-molecular interactions compared to within the
603 surrounding dilute phase. Indeed, recent studies reported that a 129- residue long
604 intrinsically disordered fragment of the human Tau protein or the prion-like low complexity
605 domain of hnRNPA1 preferentially sample more extended conformations within phase-
606 separated condensates compared to the surrounding dilute phase (Majumdar *et al*, 2019;
607 Bremer *et al*, 2021). Taken together, our data suggests that strength of inter-molecular
608 interactions regulate dynamics within condensates of PGL-3.
609
610
611 It is generally thought that chaperone proteins or RNA helicases counteract slow-down
612 of dynamics that may result from denaturation of components or inter-
613 polypeptide/RNA chain entanglements in biomolecular condensates. For instance, the
614 ATPase-dependent activity of chaperones is required to dissolve aberrant stress granules
615 that result from aggregation of misfolding-prone proteins (Ganassi *et al*, 2016; Mateju *et al*,
616 2017). In contrast, we discovered that weak interactions among two or more components
617 can buffer against large change of dynamics within the P granule phase. This effect is
618 distinct from active processes that depend on ATP hydrolysis. Specifically, we show that
619 presence of just three P granule components (PGL-1, GLH-1 and mRNA) is sufficient to
620 support a dynamic state of partially unfolded PGL-3-mEGFP within phase-separated
621 condensates. In absence of the P granule components, partially unfolded PGL-3-mEGFP
622 phase separates into non-dynamic condensates. We found that the ability of P granule
623 components to support a dynamic state of partially unfolded PGL-3-mEGFP depends on
624 the relative concentrations and hence stoichiometries of PGL-3 and the P granule
625 components. This suggests that P granule components support dynamics by participating in
626 inter-molecular interactions with PGL-3-mEGFP molecules. Similarly, different PGL-3
627 constructs – PGL-3 (K126E K129E), PGL-3 (1-452) and PGL-3 (370-693) enhanced
628 dynamics of S1 molecules within condensates to different degrees. This may correlate with
629 the varying ability of these constructs to interact with S1 molecules. We considered the
630 specificity of interactions that support fast dynamics within phase separated condensates.
631 Our data showing that different additives (P granule components, or wild-type PGL-3, or
632 PGL-3 constructs that differ in terms of their ability to fold or self-associate) can all rescue
633 slowdown of dynamics of the mutant S1 protein within condensates suggest that fast

634 dynamics can be supported by competing interactions among two or more components
635 (Fig. 6). Similarly, interactions among components could be a potential mechanism of
636 storage of misfolding-prone proteins in non-aggregated state within the liquid-like nucleolus
637 under stress in vivo (Frottin *et al*, 2019). We speculate that these interactions that support
638 fast dynamics are weak in nature and allow fast dissociation rates. Taken together, our
639 study supports the possibility that weak interactions among two or more components
640 prevent aggregation or large change of dynamics within cellular liquid-like compartments.
641
642 An interesting aspect of the dynamics buffering effect is that the dynamics of S1 remain
643 relatively unchanged regardless of the change of S1 concentration within condensates. The
644 buffering capacity depends on the additives i.e. the range of intra-condensate S1
645 concentrations where dynamics is buffered varies with additives. Once the buffering
646 capacity is exhausted i.e. beyond a threshold intra-condensate S1 concentration, dynamics
647 of S1 molecules slow down at higher S1 concentrations. More work is required to
648 understand the underlying mechanism. One possibility is that dynamics is buffered when
649 the relative concentration of S1 molecules and additives within condensates remain
650 unchanged. The “buffered” dynamics of S1 molecules within condensates also vary with
651 additives. We found that dynamics of S1 molecules is faster in presence of P granule
652 components (PGL-1, GLH-1 and mRNA) compared to that with the mutant PGL-3 (K126E
653 K129E). Future work will reveal if the buffered dynamics depend on the number of
654 interacting species within condensates (e.g. four when PGL-1, GLH-1 and mRNA is added
655 to condensates of S1; two when PGL-3 (K126E K129E) is added to S1 condensates) in
656 addition to the strength/nature of inter-molecular interactions.
657

Fig. 6 Weak interactions among two or more components promote fast dynamics in condensates.

Cartoon shows how dynamics in condensates change with composition. Each condensate contains one or more of three different macromolecules (depicted as thread, square and hexagon) at different concentrations. Homotypic interactions among threads are strong. Other homotypic and heterotypic interactions are weak. Dynamics generally correlate inversely with concentration of strong interactors in condensates. However, within a range of low concentrations of strong interactors, heterotypic interactions can buffer, at least in part, against significant change of dynamics.

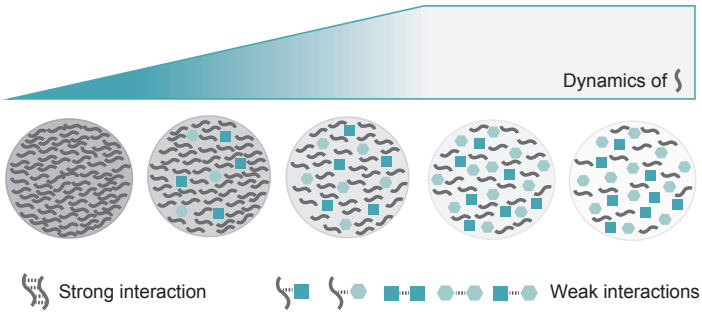

Many cellular non-membrane-bound compartments have been characterized to contain two or more phases with distinct biophysical properties (Banani *et al*, 2017; Feric *et al*, 2016; Jain *et al*, 2016; Lyon *et al*, 2021; Wang *et al*, 2014). Further, within the same liquid-like phase, diffusion rates of two different components may differ from each other (Boeynaems *et al*, 2019; Mathieu *et al*, 2020; Zhang *et al*, 2015). In P granules of *C. elegans* early embryos, a gel-like phase of MEG proteins is known to associate with the liquid-like phase of PGL proteins. The gel-like phase of MEG proteins is absent from P granules of adult *C. elegans* gonads. Two recent studies suggest that association of the gel-like MEG phase changes the surface tension of the liquid-like PGL phase without changing its viscosity or the diffusion rates of PGL proteins (Folkmann *et al*, 2021; Putnam *et al*, 2019) . Taken together, one possibility is that the dynamics-buffering mechanism that we identified here adds stability to the steady-state dynamics of liquid-like phases.

An important part of our study is to show that interactions among the α-helical N-terminal domain of PGL-3 molecules can drive phase separation. Although the unstructured C-terminus is dispensable for phase separation of PGL-3, it fine-tunes the process. First, full-length PGL-3 can phase separate at concentrations lower than the α-helical N-terminus 1-452 alone (Fig. 1c), suggesting that interactions involving the C-terminus enhance the propensity of phase separation. Second, heterotypic interactions among the unstructured C-terminus of PGL-3 molecules and mRNA facilitate phase separation of PGL-3. Our data

696 is consistent with other studies which found that interactions involving both folded domains
697 and intrinsically disordered regions of proteins drive liquid-liquid phase separation to
698 assemble many cellular non-membrane-bound compartments (Guillén-Boixet *et al*, 2020;
699 Mittag & Parker, 2018; Yang *et al*, 2020).
700
701 The concept of robustness is widely understood to be essential for the ability of genetic
702 circuits to function under a wide variety of perturbations (Félix & Barkoulas, 2015). We
703 propose that one route to achieving robustness is through condensates that contribute to
704 spatial and temporal regulation over biochemical reactions. The compositional
705 heterogeneity-dependent dynamics-buffering mechanism that we identified here could add
706 robustness to biochemical reactions within condensates against the deleterious
707 consequences of stresses, short-term effects of chemical modifications, intrinsic mutational
708 changes, and the problems that arise from accumulating high local concentrations of sticky
709 molecules. The ability to buffer against these changes to dynamics not only provides
710 robustness, but these networks of interactions could also provide a source of variation that
711 enable responsiveness when conditions change.
712

713 **Materials and Methods**

714 **Protein expression and purification**

715 All PGL-3, GLH-1 and PGL-1 constructs were purified recombinantly from insect cells using
716 a baculovirus infection system. Insect cells were harvested ~72 hours after viral infection
717 and lysed. Constructs were purified from lysates using a combination of Ni-NTA affinity,
718 anion exchange and/or size exclusion chromatography as described below.

719

720 *PGL-3, PGL-1, PGL-3 (370-693) and PGL-3 (K126E K129E):* The protocol for purification of
721 PGL-3-6xHis-mEGFP has been described earlier (Saha et al., 2016). PGL-3-6xHis-RFP,
722 PGL-1-6xHis-mEGFP, PGL-3 (370-693)-6xHis-mEGFP and PGL-3 (K126E K129E)-6xHis-
723 mEGFP were purified using the same protocol.

724

725 *PGL-3 (1-452):* Insect cells expressing PGL-3 (1-452)-6xHis-mEGFP were resuspended in
726 lysis buffer (25 mM HEPES pH 7.5, 300 mM KCl, 0.3 M L-Arginine, 10 mM Imidazole, 1 mM
727 DTT added with protease inhibitor cocktail Complete EDTA-free (Roche) and lysed using
728 sonicator. The lysates were centrifuged at 21,000 x g in a JS-13.1 rotor (Beckman-Coulter),
729 and Ni-NTA Agarose resin (Macherey-Nagel) was mixed with the supernatant to capture
730 PGL-3 protein molecules. The resin was then washed with 25 mM HEPES pH 7.5, 0.3 M
731 KCl, 20 mM Imidazole. Finally, the PGL-3 molecules were eluted into 25 mM HEPES pH
732 7.5, 300 mM KCl, 250 mM Imidazole.

733 In preparation for anion-exchange chromatography, the eluate from Ni-NTA column
734 was diluted 1:5 in 25 mM Tris pH 8.0, 1 mM DTT and 5 ml of Q Sepharose resin (GE
735 Healthcare) was mixed to capture PGL-3 protein molecules. After incubation for ~1 h, the
736 resin was washed with 25 mM Tris pH 8.0, 1 mM DTT buffers containing 350 mM, 500 mM
737 and 1 M KCl. The eluates in 25 mM Tris pH 8.0, 1 mM DTT buffers containing 500 mM KCl
738 and 1 M KCl were pooled together and further purified using size exclusion chromatography
739 with a TSKgel 5000PW column (Tosoh Bioscience) in 25 mM HEPES pH 7.5, 1 M KCl, 1
740 mM DTT.

741

742 *PGL-3 (1-577):* Insect cells expressing PGL-3 (1-577)-6xHis-mEGFP were resuspended in
743 lysis buffer (25 mM HEPES pH 7.25, 300 mM KCl, 10 mM Imidazole, 1 mM DTT added with
744 protease Inhibitor cocktail set III (Calbiochem) and lysed via passage through Avestin

745 Emulsiflex C5. The lysates were centrifuged at 20000 rpm in a Ti45 rotor (Beckman-
746 Coulter), and Ni-NTA Agarose resin (Qiagen) was mixed with the supernatant to capture
747 PGL-3 protein molecules. The resin was then washed with 25 mM HEPES pH 7.25, 300
748 mM KCl, 20 mM Imidazole, 1 mM DTT. Finally, the PGL-3 molecules were eluted into 25
749 mM HEPES pH 7.25, 300 mM KCl, 250 mM Imidazole.
750 In preparation for anion-exchange chromatography, the eluate from Ni-NTA column
751 was diluted 1:6 in 25 mM Tris pH 8.0, 1 mM DTT and 5-10 ml of Q Sepharose resin (GE
752 Healthcare) was mixed to capture PGL-3 protein molecules. After incubation for ~1 h, the
753 resin was washed with 25 mM Tris pH 8.0, 1 mM DTT buffers containing 100 mM, 200 mM,
754 350 mM, 500 mM and 1 M KCl. The PGL-3 molecules eluted into the 25 mM Tris pH 8.0, 1
755 mM DTT buffers containing 500 mM KCl and 1 M KCl.
756 The eluates were further purified using size exclusion chromatography with HiLoad
757 16/60 Superdex 200 column (GE Healthcare) in 25 mM HEPES pH 7.5, 0.3 M KCl, 1 mM
758 DTT. The fractions containing pure PGL-3 (1-577)-6xHis-mEGFP from both runs were
759 pooled together.
760
761 *S1 and S1(K126E K129E):* Insect cells expressing PGL-3 (S1)-6xHis-mEGFP or PGL-3
762 (S1(K126E K129E))-6xHis-mEGFP were resuspended in lysis buffer (25 mM HEPES pH
763 7.5, 300 mM KCl, 300 mM L-Arginine, 10 mM Imidazole, 1 mM DTT added with protease
764 inhibitor cocktail Complete EDTA-free (Roche) and lysed using sonicator. The lysates were
765 centrifuged at 21,000 x g in a JS-13.1 rotor (Beckman-Coulter), and Ni-NTA Agarose resin
766 (Macherey-Nagel) was mixed with the supernatant to capture PGL-3 protein molecules. The
767 resin was then washed with 25 mM HEPES pH 7.5, 1 M KCl, 20 mM Imidazole. Finally, the
768 PGL-3 molecules were eluted into 25 mM HEPES pH 7.5, 1 M KCl, 250 mM Imidazole.
769 Next, 500 units of Benzonase nuclease and 1 mM each of DTT and $MgCl_2$ were added to
770 the eluate and dialyzed overnight into 25 mM HEPES pH 7.5, 1 M KCl, 1 mM DTT, 1 mM
771 $MgCl_2$.
772 In preparation for anion-exchange chromatography, the dialysate was diluted 1:13 in
773 25 mM Tris pH 8.0, 1 mM DTT and 5-10 ml of Q Sepharose resin (GE Healthcare) was
774 mixed to capture PGL-3 protein molecules. After incubation for ~1 h, the resin was washed
775 with 25 mM Tris pH 8.0, 350 mM KCl, 1 mM DTT and finally the PGL-3 molecules were
776 eluted into 25 mM Tris pH 8.0, 1 M KCl, 1 mM DTT.

777 The eluates were further purified using size exclusion chromatography with a TSKgel
778 5000PW column (Tosoh Bioscience) in 25 mM HEPES pH 7.5, 1 M KCl, 1 mM DTT.
779
780 *PGL-3 (Δ425-452):* Insect cells expressing PGL-3 (Δ425-452)-6xHis-mEGFP were
781 resuspended in lysis buffer (25 mM HEPES pH 7.25, 300 mM KCl, 300 mM L-Arginine, 10
782 mM Imidazole, 1 mM DTT, 10 mM $MgCl_2$ added with protease Inhibitor cocktail set III
783 (Calbiochem) and Benzonase nuclease) and lysed via passage through Avestin Emulsiflex
784 C5. The lysates were centrifuged at 20000 rpm in a Ti45 rotor (Beckman-Coulter), and Ni-
785 NTA Agarose resin (Qiagen) was mixed with the supernatant to capture PGL-3 protein
786 molecules. The resin was then washed with 25 mM HEPES pH 7.25, 1 M KCl, 40 mM
787 Imidazole, 1 mM DTT. Finally, the PGL-3 molecules were eluted into 25 mM HEPES pH
788 7.25, 1 M KCl, 250 mM Imidazole, 1 mM DTT. Next, ~250 units of Benzonase nuclease and
789 10 mM $MgCl_2$ were added to the eluate and dialyzed overnight into 25 mM HEPES pH 7.25,
790 1 M KCl, 1 mM DTT, 10 mM $MgCl_2$.
791 In preparation for anion-exchange chromatography, the dialysate was diluted 1:12 in
792 25 mM Tris pH 8.0, 1 mM DTT and 5-10 ml of Q Sepharose resin (GE Healthcare) was
793 mixed to capture PGL-3 protein molecules. After incubation for ~1 h, the resin was washed
794 with 25 mM Tris pH 8.0, 320 mM KCl, 1 mM DTT and the PGL-3 (Δ425-452) molecules
795 were eluted into 25 mM Tris pH 8.0, 500 mM KCl, 1 mM DTT. Finally, the eluate containing
796 purified PGL-3 (Δ425-452)-6xHis-mEGFP was dialyzed into 25 mM HEPES pH 7.5, 1 M
797 KCl, 1 mM DTT.
798
799 *GLH-1*: Insect cells expressing GLH-1-6xHis-mEGFP were resuspended in lysis buffer (25
800 mM HEPES pH 7.5, 300 mM KCl, 10 mM Imidazole, 1 mM DTT added with protease
801 inhibitor cocktail Complete EDTA-free (Roche) and lysed using sonicator. The lysates were
802 centrifuged at 21,000 x g in a JS-13.1 rotor (Beckman-Coulter), and Ni-NTA Agarose resin
803 (Macherey-Nagel) was mixed with the supernatant to capture PGL-3 protein molecules. The
804 resin was then washed with 25 mM HEPES pH 7.5, 300 mM KCl, 20 mM Imidazole. Finally,
805 the GLH-1 molecules were eluted into 25 mM HEPES pH 7.5, 300 mM KCl, 250 mM
806 Imidazole.
807 In preparation for anion-exchange chromatography, the eluate was diluted 1:6 in 25
808 mM Tris pH 8.0, 1 mM DTT and 4 ml of Q Sepharose resin (GE Healthcare) was mixed to

809 capture GLH-1 protein molecules. After incubation for ~30 min, the resin was washed with
810 25 mM Tris pH 8.0, 1 mM DTT buffers containing 200 mM, 250 mM, 300 mM, 350 mM, 400
811 mM, 500 mM and 1 M KCl. The fractions with 250 to 350 mM KCl were pooled.
812 Pooled fractions were further purified using size exclusion chromatography with a
813 HiLoad 16/60 Superdex 200 column (GE Healthcare) in 25 mM HEPES pH 7.5, 300 mM
814 KCl, 1 mM DTT.
815
816 *Untagged PGL-3, S1, PGL-3 (1-452), PGL-3 (370-693), PGL-3 (K126E K129E), S1 (K126E*
817 *K129E), PGL-1 and GLH-1* were purified by cleaving off 6xHis and mEGFP tags from the
818 C-terminus of the recombinant proteins using 6xHis-tagged TEV protease, followed by
819 incubation with Ni-NTA Agarose resin to remove 6xHis-tagged mEGFP and TEV protease.
820
821 **Size exclusion chromatography and multi-angle light scattering**
822
823 Molecular weight analysis of PGL-3 (1-452) was carried out using an OMNISEC multi-
824 detector instrument from Malvern Panalytical. All measurements were performed in 25 mM
825 HEPES, 300 mM KCl, 1mM TCEP at 25°C. Prior to measurement, samples were
826 centrifuged at 10 000 g for 10 min. 90 µl of sample at 0.5 mg/ml was injected onto a
827 Superose 6 10/300 column (Cytiva). The eluate from the column was fed into a refractive
828 index detector followed by a right-angle light scattering detector (640 nm). Data were
829 analysed using the OMNISEC software (v11.10) using a refractive index increment (dn/dc)
830 of 0.185 ml/g. Bovine serum albumin (PierceTM) was used to calibrate the detectors.
831 Samples were measured in duplicate.
832
833 **Labeling of proteins with fluorescent dye**
834 In order to generate fluorescently labeled S1, PGL-1 and GLH-1, the proteins were first
835 dialyzed into buffer containing 1 mM TCEP and then incubated with AlexaFluor 594 C5-
836 maleimide (Invitrogen) in 25 mM HEPES pH 7.5, 300 mM KCl (1 M KCl for S1), 1 mM
837 TCEP for 2 h at room temperature. To remove unbound dye, repeated buffer exchange was
838 performed with 25 mM HEPES pH 7.5, 300 mM KCl (1 M KCl for S1), 1 mM TCEP until no
839 fluorescence was detected in the flow through.
840

841 **Preparation of mRNA used in experiments**

842 In order to track the localization of mRNA in our assays, fluorescently labeled mRNA was
843 generated using in vitro transcription. Coding sequence of the act-4 gene from *C. elegans*
844 was cloned to be transcribed from a T7 promoter. To generate in vitro transcribed act-4
845 mRNA, T7 RNA polymerase (New England BioLabs) was used and ribonucleotide solution
846 mix was doped with 30% Aminoallyl-UTP-Cy5 (Jena Bioscience). The reaction was
847 incubated for 1 h at 37 °C, then treated with DNase II and mRNA was finally purified using
848 RNeasy Mini Kit (Qiagen). For all the other experiments, total mouse liver mRNA (Takara)
849 was used.

850

851 **Imaging and fluorescence recovery after photobleaching (FRAP) experiments**

852 Phase separation properties of PGL-3 constructs under various conditions were imaged
853 within chambers created by attaching cover glass to glass slide with imaging spacer
854 between them (Grace Bio-Labs SecureSeal, Sigma Aldrich). 4 µL of solution was placed at
855 the center of the imaging chamber, such that the spacer had no contact with the solution.
856 PGL-3 (1-452) (Fig. 1b) was imaged directly on the cover glass (without glass slide), as
857 condensates of PGL-3 (1-452) were not stable when imaged within the glass chamber.
858 Addition of 1% crowding agent PEG-35000 stabilized condensates of this N-terminal
859 fragment of PGL-3 allowing imaging over time (Fig. 1c-e, 2a, 2b, Supplementary Fig. 2d).
860 The surfaces of glass slide and cover glass were passivated through PEG-silanization as
861 described earlier (Alberti et al., 2018).

862

863 The images were acquired with an inverted microscope (Olympus IX83) equipped with a
864 spinning-disk scan head (4,000 rpm, Yokogawa CSU-W1), a sCMOS camera (pixel size
865 11um, Prime 95B Teledyne Photometrics), and a 100x/1.4 oil-immersion objective
866 (Olympus UPLSAPO). For imaging and FRAP experiments, we used Coherent OBIS lasers
867 of wavelengths 405nm (FRAP), 488 nm, 561 nm, and 640 nm. Single confocal plane was
868 imaged over time for all FRAP experiments.

869

870 Phase separation properties of the PGL-3 constructs PGL-3 (1-577), PGL-3 (∆425-452) and
871 FRAP experiments of preheated PGL-3-mEGFP and S1-mEGFP were imaged within flow
872 chambers created by attaching cover glass to glass slide with two double-sided tapes (~60

873 μm thick) positioned parallel to each other. The surface of the cover glass was passivated
874 through PEG-silanization or coating with lipids as described earlier (Alberti et al., 2018). An
875 inverted spinning-disk confocal imaging system was used, fitted with diode-pumped solid-
876 state LASERs (wavelength 488 nm and 561 nm), Olympus UplanSApochromat 100x 1.4
877 NA oil-immersion objective, Yokogawa CSU-X1 (5000 rpm) spinning-disk scan head, and
878 Andor iXon DU-897 BV back illuminated EMCCD camera.
879
880 **Image analysis**
881 All image analysis was conducted using the Fiji image-processing package (http://fiji.sc/Fiji).
882 Images used for analysis of FRAP experiments were corrected for camera noise and
883 uneven illumination error. Intensities of the bleached areas were corrected for bleaching
884 and normalized to prebleached image. FRAP data was fitted to single exponential function
885 using Matlab (Supplementary figure 5e). All fits had R^2 value of 0.92 or higher.
886
887 FRAP data for the construct S1(K126E K129E) was acquired with the same spinning-disk
888 confocal imaging system as all other constructs, but a different FRAP filter was used. To
889 account for any difference in signal intensity resulting from the use of a different FRAP filter,
890 we compared the fluorescence intensities of S1-mEGFP, PGL-3-mEGFP and a uniformly
891 green fluorescent slide (Chroma Autofluorescent Plastic Slides) in images acquired using
892 the two different FRAP filters. This analysis using three different samples all gave similar
893 values of correction factor around 2.6. We used this correction factor to normalize the
894 intensities of S1(K126E K129E) and plotted the results in Fig. 5c.
895
896 **Phase separation assays**
897 For phase separation assays, different recombinantly-purified PGL-3 constructs were used,
898 and phase separation was triggered by diluting salt (KCl) concentration to either 150 mM or
899 100 mM in 25 mM HEPES, pH 7.5, 1 mM DTT. Following phase separation, condensates of
900 PGL-3 (1-452) dissolved rapidly when incubated within glass-based imaging chambers.
901 Addition of 1% crowding agent PEG-35000 stabilized condensates of this N-terminal
902 fragment of PGL-3 allowing imaging over time.
903

904 In some cases, PGL-3 constructs were preheated at higher temperatures (43.5 °C or 50 °C)
905 for 10 min, followed by incubation at room temperature for 10 mins and phase separation
906 via dilution of salt concentration. Incubation at higher temperatures was carried out in a
907 temperature-controlled water bath or PCR thermocycler. Heating untagged wild-type PGL-3
908 and the mutant S1 protein at 50 °C or 43.5 °C respectively resulted in aggregation. In
909 contrast, presence of mEGFP tag reduced the extent of heat-induced aggregation to a large
910 extent. Therefore, we used mEGFP-tagged PGL-3 constructs in these assays. Following
911 incubation at 43.5 °C or 50 °C, we centrifuged the samples (5 min at 20,000 g) to separate
912 the aggregates from the pool of soluble protein in the supernatant. To account for loss of
913 protein via aggregation, we remeasured the concentration of protein in the supernatant and
914 used this pool of mEGFP-tagged PGL-3 constructs for our assays.
915
916 In assays investigating phase separation of two or more components (i.e. PGL-3, S1,
917 different PGL-3 constructs, PGL-1, GLH-1 or mRNA), the components were mixed with
918 each other before phase separation was triggered by diluting the salt (KCl) to final
919 concentration of 100 mM in 25 mM HEPES pH 7.5, 1 mM DTT. In experiments where we
920 studied the correlation between concentration of S1 or PGL-3 in condensates and their half-
921 time of FRAP recovery: 1) all tested mixtures contained the same concentration of S1 (5
922 μM) or PGL-3 (5 μM) and 5% of the protein pool of S1 or PGL-3 was mEGFP-tagged; 2)
923 Image acquisition settings were the same for all the experimental groups: 50 ms exposure;
924 488-laser power set to 100%; bleaching power set to 100%.
925
926 We used fluorescently labeled PGL-3 constructs, PGL-1, GLH-1 or act-4 mRNA to check if
927 they colocalize with S1 or PGL-3 in condensates. All components were mixed with each
928 other before phase separation was triggered by diluting the salt (KCl) to final concentration
929 of 100 mM in 25 mM HEPES pH 7.5, 1 mM DTT. In these experiments, 5% of the pool of
930 PGL-3 or S1 proteins was fluorescently labeled. 100% of the other components in the mix
931 were labeled with a fluorescent probe. Colocalization of different PGL-3 constructs with
932 wild-type PGL-3 or S1 was tested by adding the different proteins in equal amounts (final
933 concentration of each component was 5 μM). In experiments where colocalization of
934 different P granule components with PGL-3 or S1 was assayed, concentration (or
935 concentration ratio) of the different components were the same as in FRAP experiments

936 (6.7 μM PGL-1, and 14 ng/ μL mRNA with 5 μM S1 or 5 μM PGL-3; 1 μM GLH-1 with 5 μM
937 PGL-3; 2 μM GLH-1 with 10 μM S1).
938
939 **Microinjection of recombinant proteins into *C. elegans* gonads**
940 Recombinant PGL-3 constructs were microinjected into gonads of young adult *C. elegans*
941 to study 1) their colocalization with P granules, and 2) the effect of the P granule phase on
942 their dynamics. To study colocalization, mEGFP-tagged PGL-3 constructs were injected
943 into gonads of worms expressing PGL-3-mCherry from the native locus (to track P
944 granules). Concentrations of injected proteins: PGL-3-mEGFP (10 μM), S1-mEGFP (6 μM)
945 and PGL-3-mEGFP preheated at 50 °C (30 μM). To minimize the effect of fluorescent tag
946 on dynamics, FRAP experiments were conducted on N2 worms microinjected with mEGFP-
947 tagged PGL-3 constructs. Concentration of injected proteins: PGL-3-mEGFP (20 μM), S1-
948 mEGFP (25 μM) and PGL-3-mEGFP preheated at 50 °C (30 μM). Worms were immobilized
949 using 2 mM levamisole and imaged immediately following injections.
950
951 **Circular Dichroism (CD) spectroscopy**
952 CD spectroscopy of PGL-3 constructs was carried out in a quartz cuvette (0.5 mm
953 pathlength) using Chirascan Plus spectrometer (Applied Photophysics) equipped with TC1
954 temperature controller (Quantum Northwest). To measure the change in α- helical content
955 of PGL-3 at different temperatures (data presented in Fig. 3b), the temperature of the
956 cuvette was varied from 20 °C to 90 °C in 2 °C steps. At each temperature, the system was
957 allowed to equilibrate for 180 s before measurement of CD signal between 200 and 260
958 nm. To test if unfolding of PGL-3 constructs at higher temperature is reversible once the
959 temperature is lowered (data presented in Supplementary Fig. 3h and i), CD signal was
960 measured initially at 21 °C, followed by measurements at a higher temperature (43.5 °C or
961 50 °C) and once again after the temperature was lowered back to 21 °C. At each
962 temperature, the system was allowed to equilibrate for 15 min before measurement of CD
963 signal between 200 and 260 nm.
964
965 **Acknowledgments**
966 We thank Anthony A. Hyman, Rohit V. Pappu, and Carsten Hoege for feedback on the
967 manuscript and helpful discussions. We thank Anthony A. Hyman and Carsten Hoege for

968 the *C. elegans* strain TH623. We thank Jana Sipkova, Anoop Kumar Yadav and Felicitas
969 Arlt for help with image analysis and technical support. S.S. initiated this study as a
970 postdoctoral fellow in the lab of A.A. Hyman. We thank the services and facilities at Vienna
971 BioCenter for support - IMBA BioOptics Facility for support with imaging; IMBA Molecular
972 Biology Service for providing reagents for cloning and recombinant protein purification, and
973 sequencing of constructs; VBCF Protein Technologies for help with recombinant protein
974 expression and performing SEC-MALS experiment; IMBA Protein Chemistry Facility for
975 verification of recombinant proteins using mass spectrometry. S.J., J.B., P.C., B.R.P., and
976 S.S. are funded by the Austrian Academy of Sciences. A.S.H. is scientific advisor at
977 Dewpoint Therapeutics.
978
979 **Author contribution:** Conceptualization, S.J. and S.S.; Methodology, S.J., A.S.H. and
980 S.S.; Investigation, S.J., J.B., P.C., B.R.P., M.R., S.S.; Writing – Original Draft, S.J. and
981 S.S.; Writing – Review & Editing, S.J., A.S.H., and S.S.; Funding Acquisition, S.S.;
982 Resources, A.S.H. and S.S.; Supervision, S.S.
983

984 **References**

985 Alshareedah I, Thurston GM & Banerjee PR (2021) Quantifying viscosity and surface
986 tension of multicomponent protein-nucleic acid condensates. *Biophysical Journal*
987 120: 1161–1169

988 Aoki ST, Kershner AM, Bingman CA, Wickens M & Kimble J (2016) PGL germ granule
989 assembly protein is a base-specific, single-stranded RNase. *Proceedings of the*
990 *National Academy of Sciences of the United States of America*

991 Aoki ST, Lynch TR, Crittenden SL, Bingman CA, Wickens M & Kimble J (2021) C. elegans
992 germ granules require both assembly and localized regulators for mRNA repression.
993 *Nat Commun* 12: 996

994 Banani SF, Lee HO, Hyman AA & Rosen MK (2017) Biomolecular condensates: organizers
995 of cellular biochemistry. *Nature reviews Molecular cell biology* 18: 285–298

996 Banani SF, Rice AM, Peeples WB, Lin Y, Jain S, Parker R & Rosen MK (2016)
997 Compositional Control of Phase-Separated Cellular Bodies. *Cell* 166: 651–663

998 Boeynaems S, Holehouse AS, Weinhardt V, Kovacs D, Van Lindt J, Larabell C, Van Den
999 Bosch L, Das R, Tompa PS, Pappu RV, *et al* (2019) Spontaneous driving forces give
1000 rise to protein-RNA condensates with coexisting phases and complex material
1001 properties. *Proceedings of the National Academy of Sciences of the United States of*
1002 *America* 116: 7889–7898

1003 Brangwynne CP, Eckmann CR, Courson DS, Rybarska A, Hoege C, Gharakhani J, Jülicher
1004 F & Hyman AA (2009) Germline P granules are liquid droplets that localize by
1005 controlled dissolution/condensation. *Science* 324: 1729–1732

1006 Bremer A, Farag M, Borcherds WM, Peran I, Martin EW, Pappu RV & Mittag T (2021)
1007 Deciphering how naturally occurring sequence features impact the phase behaviors
1008 of disordered prion-like domains Biophysics

1009 Choi J-M, Holehouse AS & Pappu RV (2020) Physical Principles Underlying the Complex
1010 Biology of Intracellular Phase Transitions. *Annual review of biophysics* 49: 107–133

1011 Félix M-A & Barkoulas M (2015) Pervasive robustness in biological systems. *Nature*
1012 *Reviews Genetics* 16: 483–496

1013 Feric M, Vaidya N, Harmon TS, Mitrea DM, Zhu L, Richardson TM, Kriwacki RW, Pappu RV
1014 & Brangwynne CP (2016) Coexisting Liquid Phases Underlie Nucleolar
1015 Subcompartments. *Cell*: 1–13

1016 Folkmann AW, Putnam A, Lee CF & Seydoux G (2021) Regulation of biomolecular
1017 condensates by interfacial protein clusters. *Science* 373: 1218–1224

1018 Frottin F, Schueder F, Tiwary S, Gupta R, Körner R, Schlichthaerle T, Cox J, Jungmann R,
1019 Hartl FU & Hipp MS (2019) The nucleolus functions as a phase-separated protein
1020 quality control compartment. *Science* 365: 342–347

1021 Ganassi M, Mateju D, Bigi I, Mediani L, Poser I, Lee HO, Seguin SJ, Morelli FF, Vinet J,
1022 Leo G, *et al* (2016) A Surveillance Function of the HSPB8-BAG3-HSP70 Chaperone
1023 Complex Ensures Stress Granule Integrity and Dynamism. *Molecular cell* 63: 796–
1024 810

1025 Guillén-Boixet J, Kopach A, Holehouse AS, Wittmann S, Jahnel M, Schlüßler R, Kim K,
1026 Trussina IREA, Wang J, Mateju D, *et al* (2020) RNA-Induced Conformational
1027 Switching and Clustering of G3BP Drive Stress Granule Assembly by Condensation.
1028 *Cell* 181: 346-361.e17

1029 Hanazawa M, Yonetani M & Sugimoto A (2011) PGL proteins self associate and bind RNPs
1030 to mediate germ granule assembly in C. elegans. *The Journal of Cell Biology* 192:
1031 929–937

1032 Jain S, Wheeler JR, Walters RW, Agrawal A, Barsic A & Parker R (2016) ATPase-
1033 Modulated Stress Granules Contain a Diverse Proteome and Substructure. *Cell* 164:
1034 487–498

1035 Jawerth L, Fischer-Friedrich E, Saha S, Wang J, Franzmann T, Zhang X, Sachweh J, Ruer
1036 M, Ijavi M, Saha S, *et al* (2020) Protein condensates as aging Maxwell fluids.
1037 *Science* 370: 1317–1323

1038 Klosin A, Oltsch F, Harmon T, Honigmann A, Jülicher F, Hyman AA & Zechner C (2020)
1039 Phase separation provides a mechanism to reduce noise in cells. *Science* 367: 464–
1040 468

1041 Lyon AS, Peeples WB & Rosen MK (2021) A framework for understanding the functions of
1042 biomolecular condensates across scales. *Nat Rev Mol Cell Biol* 22: 215–235

1043 Majumdar A, Dogra P, Maity S & Mukhopadhyay S (2019) Liquid-Liquid Phase Separation
1044 Is Driven by Large-Scale Conformational Unwinding and Fluctuations of Intrinsically
1045 Disordered Protein Molecules. *The Journal of Physical Chemistry Letters* 10: 3929–
1046 3936

1047 Mateju D, Franzmann TM, Patel A, Kopach A, Boczek EE, Maharana S, Lee HO, Carra S,
1048 Hyman AA & Alberti S (2017) An aberrant phase transition of stress granules
1049 triggered by misfolded protein and prevented by chaperone function. *The EMBO*
1050 *journal* 36: 1669–1687

1051 Mathieu C, Pappu RV & Taylor JP (2020) Beyond aggregation: Pathological phase
1052 transitions in neurodegenerative disease. *Science* 370: 56–60

1053 Mittag T & Parker R (2018) Multiple Modes of Protein-Protein Interactions Promote RNP
1054 Granule Assembly. *Journal of molecular biology* 430: 4636–4649

1055 Putnam A, Cassani M, Smith J & Seydoux G (2019) A gel phase promotes condensation of
1056 liquid P granules in Caenorhabditis elegans embryos. *Nat Struct Mol Biol* 26: 220–
1057 226

1058 Rhine K, Makurath MA, Liu J, Skanchy S, Lopez C, Catalan KF, Ma Y, Ha T, Chemla YR &
1059 Myong S (2020) ALS/FTLD-Linked Mutations in FUS Glycine Residues Cause
1060 Accelerated Gelation and Reduced Interactions with Wild-Type FUS. *Molecular cell*

1061 Riback JA, Zhu L, Ferrolino MC, Tolbert M, Mitrea DM, Sanders DW, Wei M-T, Kriwacki
1062 RW & Brangwynne CP (2020) Composition-dependent thermodynamics of
1063 intracellular phase separation. *Nature* 581: 209–214

1064 Saha S, Weber CA, Nousch M, Adame-Arana O, Hoege C, Hein MY, Osborne Nishimura E,
1065 Mahamid J, Jahnel M, Jawerth L, *et al* (2016) Polar Positioning of Phase-Separated
1066 Liquid Compartments in Cells Regulated by an mRNA Competition Mechanism. *Cell*
1067 166: 1572-1584.e16

1068 Sanders DW, Kedersha N, Lee DSW, Strom AR, Drake V, Riback JA, Bracha D, Eeftens
1069 JM, Iwanicki A, Wang A, *et al* (2020) Competing Protein-RNA Interaction Networks
1070 Control Multiphase Intracellular Organization. *Cell* 181: 306-324.e28

1071 Updike D & Strome S (2010) P granule assembly and function in Caenorhabditis elegans
1072 germ cells. *Journal of andrology* 31: 53–60

1073 Wang JT, Smith J, Chen B-C, Schmidt H, Rasoloson D, Paix A, Lambrus BG, Calidas D,
1074 Betzig E & Seydoux G (2014) Regulation of RNA granule dynamics by
1075 phosphorylation of serine-rich, intrinsically disordered proteins in C. elegans. *eLife* 3:
1076 449–23

1077 Yang P, Mathieu C, Kolaitis R-M, Zhang P, Messing J, Yurtsever U, Yang Z, Wu J, Li Y,
1078 Pan Q, *et al* (2020) G3BP1 Is a Tunable Switch that Triggers Phase Separation to
1079 Assemble Stress Granules. *Cell* 181: 325-345.e28

1080 Zhang H, Elbaum-Garfinkle S, Langdon EM, Taylor N, Occhipinti P, Bridges AA,
1081 Brangwynne CP & Gladfelter AS (2015) RNA Controls PolyQ Protein Phase
1082 Transitions. *Molecular cell* 60: 220–230

1083

Supplementary Information

Supplementary Figure 1

SDS-PAGE of recombinantly-purified proteins used in this study. Four SDS-PAGE gels are shown (gel 1: lanes 1-13; gel 2: lanes 14-20; gel 3: lanes 21-23, gel 4: lanes 24-26). Lane 21 is not adjacent to lanes 22 and 23 in gel 3; lanes 24, 25 and 26 represent non-adjacent lanes in gel 4.

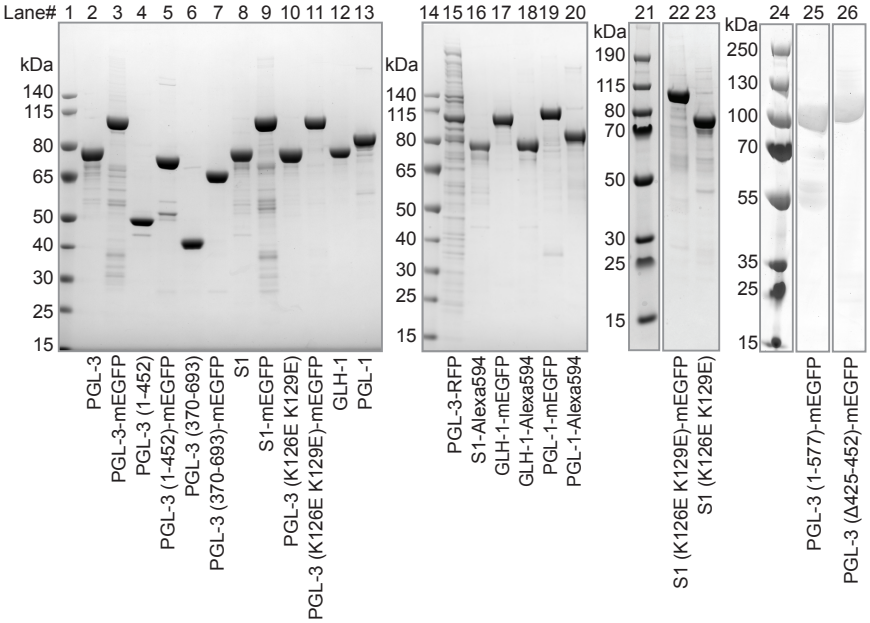

Supplementary Figure 2

a Sequence of PGL-3 with secondary structure highlighted in different colors as predicted by the web-based PSIPRED 4.0 server. Dark grey β strand, blue: α helix, light grey: coil. (http://bioinf.cs.ucl.ac.uk/psipred/).
b Plot of disorder probability across the length of PGL-3, as predicted by the web-based PrDOS (Protein DisOrder prediction System) server with false-positive rate of 5.0% (http://prdos.hgc.jp/cgi-bin/top.cgi).
c Plot of average normalized fluorescence over time in bleached regions (1.5 μm x 1.5 μm) within condensates of PGL-3 alone (black circles, 10 μM, 5% mEGFP-tagged, n = 18), or PGL-3 (blue circles, 5 μM, 5% mEGFP-tagged, n = 21) in presence of PGL-1 (6.7 μM), GLH-1 (1 μM) and total mRNA (14 ng/μL). Error bars represent 1 SD.
d Time-lapse fluorescence micrographs show fluorescence recovery over time after a condensate of PGL-3 (1-452) (5 μM, 5% mEGFP-tagged) was photobleached. Scale bar 5 μm. Below is shown a plot of average normalized fluorescence over time in 11 condensates of PGL-3 (1-452) (21 μM, 5% mEGFP-tagged) that were photobleached. Error bars represent 1 SD.
e Bright field micrograph of PGL-3 (1-452) (5 μM) in 25 mM HEPES pH 7.5, 100 mM KCl, 1 mM DTT. Scale bar 20 μm.
f Representative plot of size exclusion chromatography and multi-angle light scattering (SEC-MALS) data for PGL-3 (1-452). Black: relative refractive index response (Y-axis, left), Grey: molecular weight in kDa (Y- axis, right). Measurements were performed in 25 mM HEPES, 300 mM KCl, 1 mM TCEP. Average molecular weight of PGL-3 (1-452) estimated from SEC-MALS is 109.5 (±1.4) kDa (n = 2). Expected molecular weight based on amino acid sequence is 50.5 kDa, suggesting that PGL-3 (1-452) exists as a dimer.
g Plot of average normalized fluorescence over time in bleached regions (1.5 μm x 1.5 μm) within condensates of PGL-3 (black circles, 5% mEGFP-tagged, n = 18), PGL-3 (1-452) (blue circles, 5% mEGFP-tagged, n = 24) and PGL-3 (1-577)-mEGFP (grey circles, bleached region 1.4 μm x 1.4 μm, n = 8). Error bars represent 1 SD.

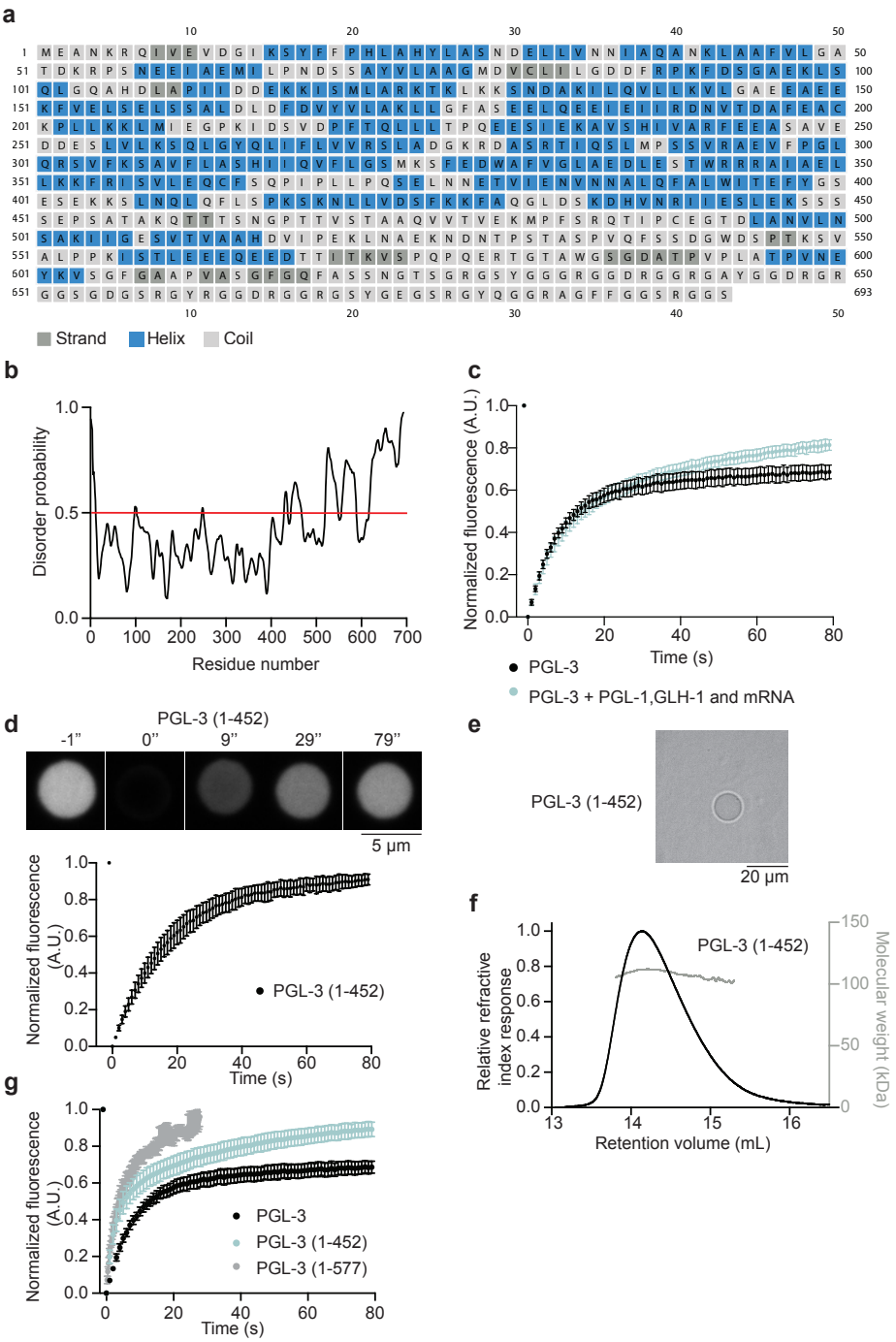

Supplementary Figure 3

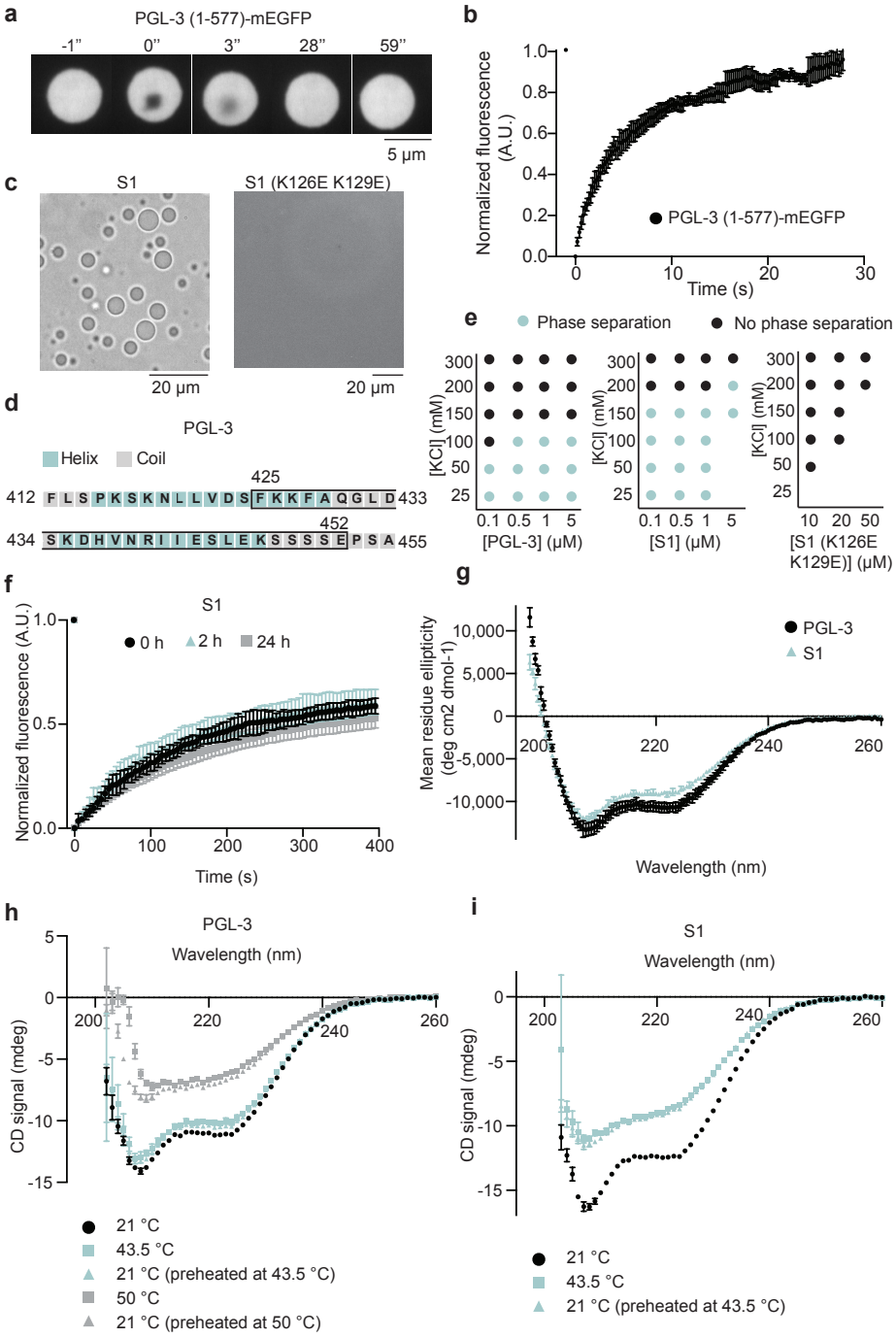

a Time-lapse fluorescence micrographs show fluorescence recovery over time after a 1.4 µm x 1.4 µm area within a condensate of PGL-3 (1-577)-mEGFP (20 µM) was photobleached. Scale bar 5 µm.
b Plot showing average normalized fluorescence of bleached region (1.4 µm x 1.4 µm) within PGL-3 (1-577)-mEGFP condensates (n=8) over time. Error bars represent 1 SD.
c Bright-field micrographs of S1 (8 µM) in 25 mM HEPES pH 7.5, 100 mM KCl, 1 mM DTT and S1 (K126E K129E) (50 µM) in 25 mM HEPES pH 7.5, 150 mM KCl, 1 mM DTT. Scale bar 20 µm.
d Sequence of PGL-3 (412-455) with secondary structure highlighted in different colors as predicted by the web-based PSIPRED 4.0 server. Light blue: α helix, grey: coil. (http://bioinf.cs.ucl.ac.uk/psipred/). Residues 425-452 (shuffled in S1) are highlighted within open black box.
e Phase diagrams of PGL-3, S1 and S1(K126E K129E) at different protein and salt (KCl) concentrations in 25 mM HEPES pH 7.5, 1 mM DTT. Blue circles represent conditions where phase separation was observed. Black circles represent conditions where phase separation was absent. 5% of the pool of protein was tagged with mEGFP in each case.
f Plot showing average normalized fluorescence of bleached regions (1.5 µm x 1.5 µm) within condensates of S1 (10 µM, 5% mEGFP-tagged) over time. Condensates were assayed at different times after assembly via phase separation and incubation at 20 °C (Black circles: immediately following assembly (n = 16), blue triangles: 2 h post-assembly (n = 14), grey squares: 24 h post-assembly (n = 11). Error bars represent 1 SD.
g Plot of mean residue ellipticity of PGL-3 and S1 vs. wavelength assayed using circular dichroism (CD) spectroscopy. Black circles: PGL-3 (3 µM, 10 mM Potassium phosphate pH 7.5, 300 mM KCl, 1 mM TCEP), Blue triangles: S1 (3 µM, 10 mM Potassium phosphate pH 7.5, 300 mM KCl, 1 mM TCEP). Error bars represent 1 SD among six CD scans.
h-i Plots of circular dichroism signal vs. wavelength of **h** PGL-3 (3 µM) and **i** S1 (3 µM) in 25 mM HEPES pH 7.5, 1 M KCl and 1 mM DTT at different temperatures. Error bars represent 1 SD among six CD scans. Black circles: 21 °C, blue squares: 43.5 °C, blue triangles: 21 °C (after preheating at 43.5 °C), grey squares: 50 °C, grey triangles: 21 °C (after preheating at 50 °C).

Supplementary Figure 4

a Time-lapse fluorescence micrographs show fluorescence recovery after photobleaching over time in a condensate of PGL-3-mEGFP preheated at 50 °C (5 µM) in presence of PGL-1 (6.7 µM), GLH-1 (1 µM), and total mRNA (14 ng/µL). Scale bar 5 µm. Shown next to the micrographs is a plot of average normalized fluorescence over time in bleached regions (1.5 µm x 1.5 µm) within the condensates of PGL-3-mEGFP preheated at 50 °C (n = 15). Error bars represent 1 SD.
b-e Fluorescence micrographs show concentration of PGL-1, GLH-1 and act-4 mRNA (in vitro transcribed) within condensates of PGL-3 **b**, S1 **c**, PGL-3-mGFP **d** and PGL-3-mEGFP preheated at 50 °C **e**. To track condensates of PGL-3 and S1 in **b-c**, 5% of the pool of PGL-3 or S1 proteins used were tagged with RFP, mEGFP or Alexa 594. Fluorophores used to track PGL-1 (mEGFP or Alexa 594), GLH-1 (mEGFP or Alexa 594), and mRNA (Cy5) are specified in each case. Scale bars **b-d** 20 µm, **e** 10 µm.

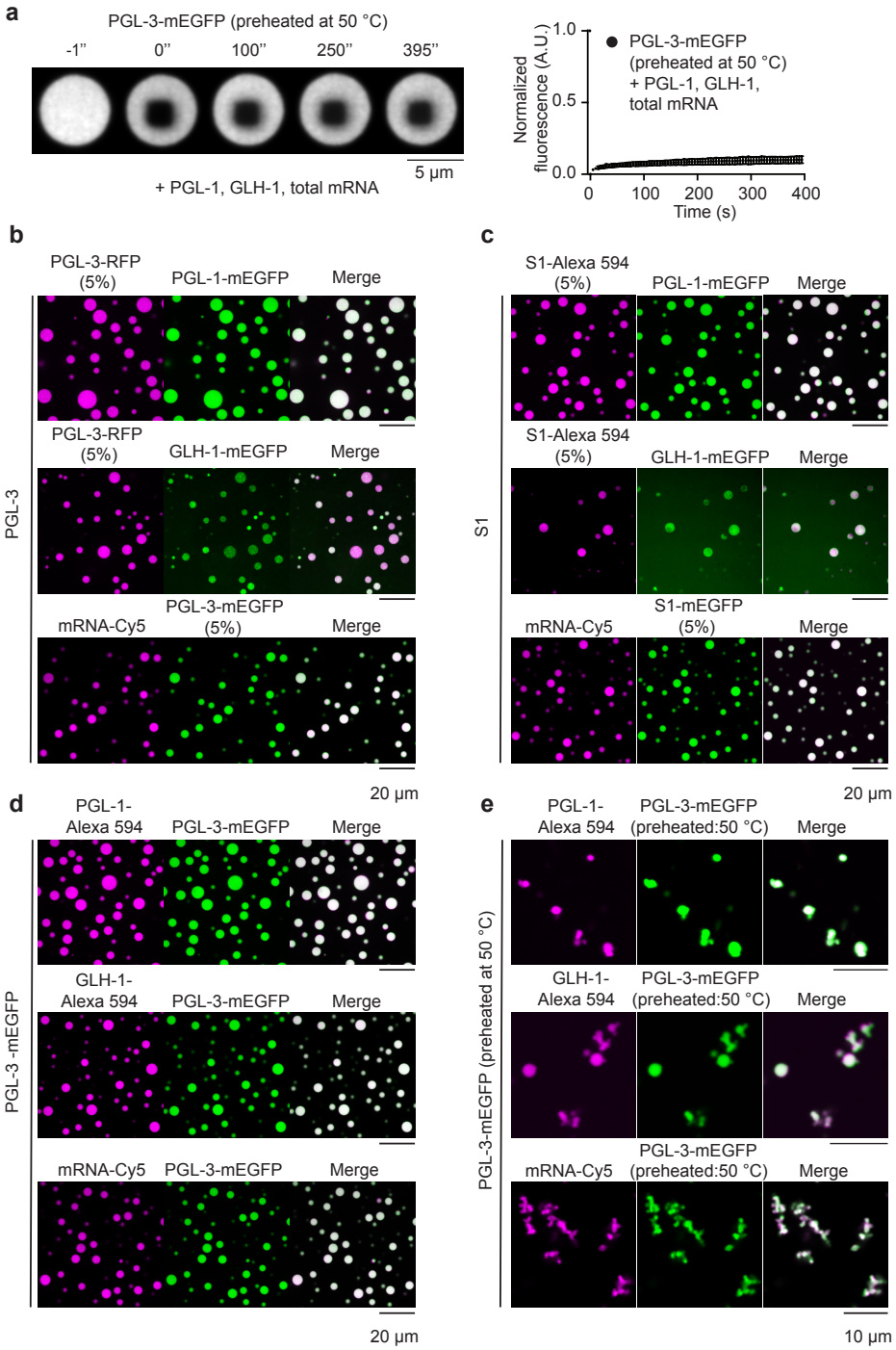

Supplementary Figure 5

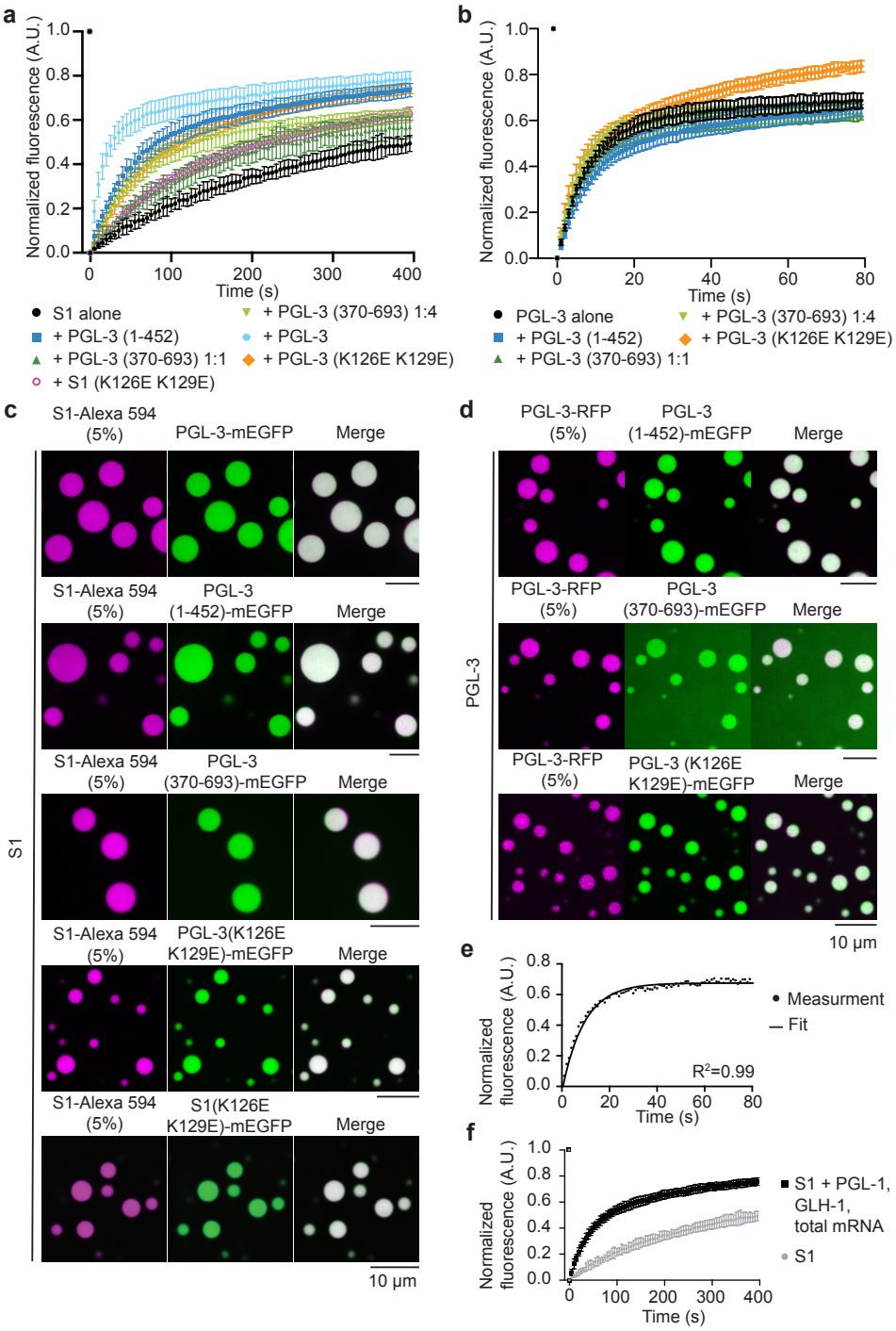

a Plot of average normalized S1-mEGFP fluorescence over time in bleached regions (1.5 µm x 1.5 µm) within the condensates of defined composition as follows. Black circles: S1 alone (10 µM, 5% mEGFP-tagged) (n = 18), light green triangle: S1 (5 µM, 5% mEGFP-tagged) + PGL-3 (370-693) (20 µM) (n = 24), blue square: S1 (5 µM, 5% mEGFP-tagged) + PGL-3 (1-452) (5 µM) (n = 16), light blue hexagon: S1 (5 µM, 5% mEGFP-tagged) + PGL-3 (5 µM) (n = 20), green triangle: S1 (5 µM, 5% mEGFP-tagged) + PGL-3 (370-693) (5 µM) (n = 11), orange diamond: S1 (5 µM, 5% mEGFP-tagged) + PGL-3 (K126E K129E) (5 µM) (n = 17), magenta open circle: S1 (5 µM, 5% mEGFP-tagged) + S1 (K126E K129E) (5 µM) (n = 13). Error bars represent 1 SD.
b Plot of average normalized PGL-3-mEGFP fluorescence over time in bleached regions (1.5 µm x 1.5 µm) within the condensates of defined composition as follows. Black circles: PGL-3 alone (10 µM, 5% mEGFP-tagged) (n = 18), light green triangle: PGL-3 (5 µM, 5% mEGFP-tagged) + PGL-3 (370-693) (20 µM) (n = 12), blue square: PGL-3 (5 µM, 5% mEGFP-tagged) + PGL-3 (1-452) (5 µM) (n = 28), green triangle: PGL-3 (5 µM, 5% mEGFP-tagged) + PGL-3 (370-693) (5 µM) (n = 13), orange diamond: PGL-3 (5 µM, 5% mEGFP-tagged) + PGL-3 (K126E K129E) (5 µM) (n =12). Error bars represent 1 SD.
c-d Fluorescence micrographs show concentration of PGL-3-mEGFP, PGL-3 (1-452)-mEGFP, PGL-3 (370-693)-mEGFP, PGL-3 (K126E K129E)-mEGFP or S1(K126E K129E)-mEGFP within condensates of S1 **c** or PGL-3 **d**. To track condensates of S1 and PGL-3 in **c-d**, 5% of the pool of S1 or PGL-3 proteins used were tagged with Alexa 594 or RFP. Scale bar 10 µm.
e A representative plot of normalized PGL-3-mEGFP fluorescence over time in bleached regions (1.5 µm x 1.5 µm) within a condensate and corresponding single exponential fit. FRAP data was fitted to the single exponential function: $y = a * (1 - \exp(-b*x))$. R^2 values were ≥ 0.92 for all fits.
f Plot of average normalized fluorescence over time in bleached regions (1.5 µm x 1.5 µm) within condensates of S1 alone (grey circle, 10 µM, 5% mEGFP-tagged, n =18), or S1 (black square, 5 µM, 5% mEGFP-tagged, n = 21) in presence of PGL-1 (6.7 µM), GLH-1 (1 µM) and total mRNA (14 ng/µL). Error bars represent 1 SD.

Supplementary Figure 6

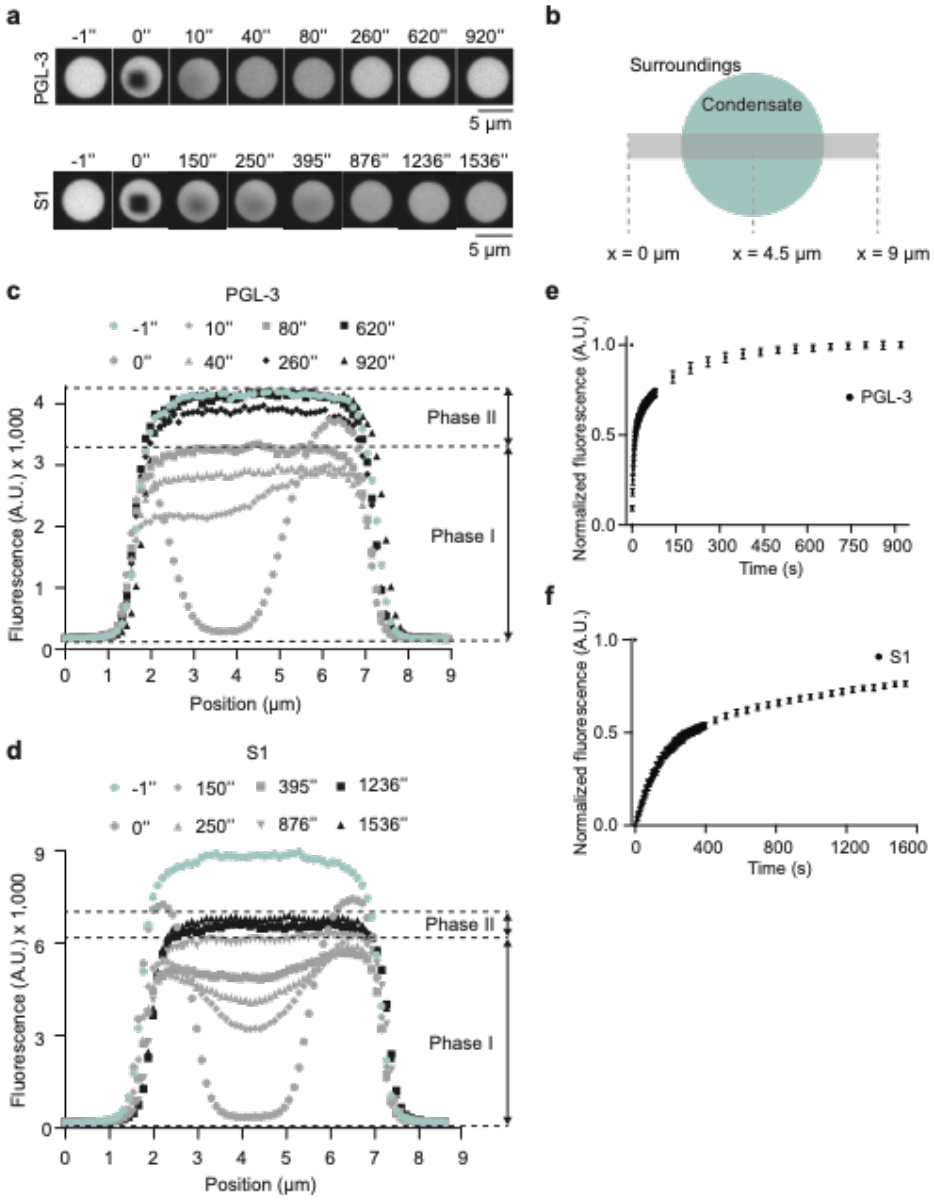

a Time-lapse fluorescence micrographs show fluorescence recovery after photobleaching over time in condensates of PGL-3 (10 µM) or S1 (10 µM) (5% of the pool of protein was tagged with mEGFP). Scale bars 5 µm.
b Cartoon defining position with respect to a condensate. This position scheme was used to generate fluorescence-profile plots shown in **c** and **d**.
c-d Profile plots mapping the fluorescence signal at different positions within a condensate of PGL-3 **c** or S1 **d**. Plots shows fluorescence signal in selected area (see **b** at different time points. Over time, fluorescence recovers within bleached regions through a combination of internal rearrangement of molecules within condensates and exchange of molecules between condensates and surroundings. Colors represent different recovery phases: blue for time before bleaching, grey for phase I and black for phase II. Phase I is a fast phase of fluorescence recovery that promotes homogenization of fluorescence signal within the condensate predominantly via internal rearrangement of molecules. Phase II is a slower phase of fluorescence recovery that depend predominantly on additional replenishment of unbleached molecules from the surroundings. Different time points are shown as follows. **c** Blue circle: -1 s (before bleaching), grey circle: 0 s (moment of bleaching), grey diamond: 10 s, grey triangle: 40 s, grey square: 80 s, black diamond: 260 s, black square: 620 s, black triangle: 920 s after bleaching. **d** Blue circle: -1 s (before bleaching), grey circle: 0 s (moment of bleaching), grey diamond: 150 s, grey triangle: 250 s, grey square: 395 s, grey reverse triangle: 876 s, black square: 1236 s, black triangle: 1536 s after bleaching.
e-f Plots of average normalized fluorescence over time in bleached regions (1.5 µm x 1.5 µm) within the condensates of PGL-3 (n = 9) **e** or S1 (n=9) **f** imaged as described in **a**. Error bars represent 1 SD.